NTNU Trondheim
Norwegian University of Science and Technology
Department of Marine Technology – Group of Marine Structures

MASTER THESIS IN MARINE TECHNOLOGY

SPRING 2017

FOR

STUD. TECHN. CARINA NORVIK

DESIGN OF ARTIFICIAL SEAWEEDS FOR ASSESSMENT OF HYDRODYNAMIC PROPERTIES OF SEAWEED FARMS

The interaction between aquatic biological systems and their physical environment represents a complexity which is important to understand for sustainable management of aquatic environments. In order to learn more about the complexity of the processes that take place in such environments, the knowledge from different disciplines have to be taken into account, from e.g. engineering, biology and ecology. Several issues need to be considered, such as the biomechanical properties of the plant, the complex fluid flow involving turbulent processes, as well as design and scaling issues related to laboratory experiments.

The thesis will focus on various issues of the representation of vegetation-flow interactions in laboratory experiments.

The student shall:

1. Give a literature review of flow and aquatic vegetation interaction.
2. Give the theoretical background for the vegetation-flow interaction as well as the interaction between individual plants, with special emphasis on design of surrogate models.
3. Perform, present and discuss results from flow experiments in a test facility using surrogate models.

The work scope may prove to be larger than initially anticipated. Subject to approval from the supervisor, topics may be deleted from the list above or reduced in extent.

In the thesis the candidate shall present her personal contribution to the resolution of problem within the scope of the thesis work.

Theories and conclusions should be based on mathematical derivations and/or logic reasoning identifying the various steps in the deduction.

The candidate should utilize the existing possibilities for obtaining relevant literature.

The thesis should be organized in a rational manner to give a clear exposition of results, assessments, and conclusions. The text should be brief and to the point, with a clear language. Telegraphic language should be avoided.

The thesis shall contain the following elements: A text defining the scope, preface, list of contents, summary, main body of thesis, conclusions with recommendations for further work, list of symbols

and acronyms, reference and (optional) appendices. All figures, tables and equations shall be numerated.

The supervisor may require that the candidate, in an early stage of the work, present a written plan for the completion of the work. The plan should include a budget for the use of computer and laboratory resources that will be charged to the department. Overruns shall be reported to the supervisor.

The original contribution of the candidate and material taken from other sources shall be clearly defined. Work from other sources shall be properly referenced using an acknowledged referencing system.

Deadline: 10.07.2017

Supervisors:
Research Scientist Andreas Myskja Lien, Sintef Ocean
Post. doc. Pierre-Yves Henry, Department of Civil and Environmental Engineering
Professor Dag Myrhaug

Dag Myrhaug
Supervisor

Preface

The field of the biomechanics and hydrodynamics of macroalgae first came to my attention in the summer of 2016, when I worked for SINTEF Ocean under the MacroSea project. I was tasked with the design of artificial seaweeds for assessment of hydrodynamic properties of seaweed farms. The seaweed in question was *Laminaria saccharina*, the sugar kelp. Having previously studied biotechnology, a task allowing me to utilize both my backgrounds was very rewarding. During the summer I realized that there was a lack of knowledge regarding the hydrodynamic properties of seaweeds, and in particularly for seaweeds with complex shapes. With the limited time available, it was therefore not possible to make simplification of the complex morphology of *L. saccharina* and still be confident that it would reproduce the hydrodynamic properties of the real seaweed. The material properties and geometry of the artificial seaweed were therefore made to be as similar to the real seaweed properties as possible. The complex shape of the artificial seaweed meant that individual models had to be cast, which is very time consuming and costly. It is therefore of interest to reduce the complexity of the models, and to work towards not having to cast individual plants, but rather be able to mass produce them by e.g. stamping out models from premade sheets or cutting strips.

The objective of this master thesis was to add knowledge regarding the hydrodynamic of seaweed for future assessment of hydrodynamic properties of seaweed farms by comparing models with simplified morphology of *L. saccharina*. The most simplified model is just a flat blade with the same outline as the complex models found during the summer 2016. The other model includes the undulate shape seen in *L. saccharina*.

Trondheim, July 9, 2017

Carina Norvik

Acknowledgment

Special thanks go to the staff working at the laboratories at Tyholt and Valgrinda; Torgeir Wahl, Trond Innset, Ole Erik Vinje, Gustav Jacobsen, Kristian Agustin Jensen and Marcus Almehagen. Without their help and guidance, the drag experiments could not have been performed. I would also like to thank master students Benedicte Elise Fløgum, Marie Flø Aarsnes and Aurélien Liné for helping me during the experiments and looking out for my safety. Additionally, I would like thank Aurélien Liné again for helping me mitigate distortion of the underwater footage. I would also like to thank head of the Marine Technology department Sverre Steen for making time in his busy schedule to meet me and answer my questions regarding similarity theory and scaling. A thanks also goes PhD-student Valentin Bruno Chabaud for discussion regarding post-processing and filtering of disturbance of drag force data. The support given to me by my room-mate Abba Elizabeth Coron has been very important to me, and should not go unmentioned. I must also thank my mother, June Bråthen, as she has always been my supporter. Finally, I would like to thank my supervisors, scientist at SINTEF Ocean Andreas Myskja Lien, post-doc Pierre-Yves Henry and professor Dag Myrhaug, for giving me guidance and helping me throughout the last year.

List of Symbols

δ_ρ	Ratio of plant density in full and model scale
δ_υ	Ratio of fluid kinematic viscosity in full and model scale
ϵ	Strain
λ	Scale parameter
μ	Dynamic viscosity
ω	Cross-sectional area
Π_i	Dimensionless ratio i
ψ	Vogel exponent
ψ_b	'Bending'-plant Vogel exponent
ψ_t	'Tensile'-plant Vogel exponent
ρ	Fluid density
ρ_p	Plant density
ρ_{pF}	Plant density in full scale
ρ_{pM}	Plant density in model scale
σ	Surface tension
Θ	Temperature

υ	Kinematic viscosity
υ_F	Kinematic viscosity in full scale
υ_M	Kinematic viscosity in model scale
A	Characteristic area
AR	Aspect ratio
b	Breadth
C	Arbitrary dimensionless constant
C'	Arbitrary constant
C_D	Drag coefficient
C_L	Lift coefficient
Ca	Cauchy number
E	Elastic modulus
E_b	Bending modulus
E_F	Elastic modulus in full scale
E_M	Elastic modulus in model scale
E_{bF}	Bending modulus in full scale
E_{bM}	Bending modulus in model scale
F	Force
F_B	Buoyancy force
F_b	Bending reaction force
F_D	Drag force

F_G	Gravity force
F_L	Lift force
f_n	Natural frequency
F_T	Tensile reaction force
Fr	Froude number
G	Modulus of elasticity in shear
g	Gravitational acceleration
g_F	Gravitational acceleration in full scale
g_M	Gravitational acceleration in model scale
I	Second moment of area
I_F	Second moment of area in full scale
I_M	Second moment of area in model scale
J	Flexural rigidity
J_F	Flexural rigidity in full scale
J_M	Flexural rigidity in model scale
KC	Keulegan-Carpenter number
L	Length
L_1	Length 1
L_2	Length 2
L_F	Length in full scale
L_M	Length in model scale

M	Mass
M_F	Mass in full scale
M_M	Mass in model scale
p	Pressure
q_i	Numerical value of quantity i
R	Radius of curvature
r	Radius
Re	Reynolds number
St	Strouhal number
T	Time
t	Thickness
T_A	Period of oscillation
T_a	Applied torque
T_F	Time in full scale
T_M	Time in model scale
U	Relative velocity
U_A	Amplitude of flow velocity oscillation
U_F	Relative velocity in full scale
U_M	Relative velocity in model scale
V	Volume
V_p	Plant volume

w Width

W_{pull} Work per volume required to pull specimen

W_{recoil} Work per volume used for elastic recoil

x Distance between holdfast and the point where the resultant fluid force acts

X_F Parameter in full scale

X_M Parameter in model scale

Summary

In recent years the prospect of having a seaweed industry in Norway has become of interest. Assessing the hydrodynamic properties of seaweed farms through experiments can help optimize its design and thereby potential amount of biomass produced. However, there are difficulties associated with using seaweeds for experimental purposes, such as deterioration of the biological material when exposed to environments different from where they were harvested. Moreover, many facilities do not allow for biological material to be introduced. Consequently, to be able to assess hydrodynamic properties of seaweed farms, artificial seaweeds that accurately replicate important features of seaweed biomechanics and hydrodynamics are needed. It is important that the these properties are correctly reproduced on both blade and patch scale.

The objective of this master thesis was to add to the knowledge of the hydrodynamics of seaweeds, more specifically *Laminaria saccharina*, the sugar kelp, to help future assessment of the hydrodynamic properties of seaweed farms. This was done by comparing drag force and behavior of two simplified blade morphologies, flat and undulate, both with uniform thickness. Even though seaweeds are subjected to both current and wave action, wave action was outside of the scope of this master thesis, and only steady, uni-directional flow was be considered. The experiments were conducted in the Marine Cybernetics laboratory at Department of Marine Technology at NTNU. The laboratory has equipment allowing for towing experiments. Two setups were use, one with only a profiled rod piercing the surface and one with a cylinder attached that allowed for dye to be distributed along its surface. The models were attached to the lower ends of the setups, and both blade and patch scale were considered. Two model sizes were tested for each simplified morphology. Due to high amounts of vibration and noise, the raw data was filtered before mean values and development of the drag force were presented. Underwater video footage allowed for some visual cues and behaviors to be observed and compared with the drag force.

The main finding of this master thesis, was that in contrary to the findings of Vettori (2016), flat blades do not seem to be a good representation of the undulate kelp *L. saccharina*. Agreeing with the findings of Paul and Henry (2014), it is likely that the models behave differently from the real seaweed due to different material density and therefore buoyancy. The reason for this

conclusion can be seen from the video footage, showing that the models were behaving more similarly to a 'bending' plant rather than a 'tensile' plant at lower velocities. The Vogel exponent also had distinctly different behavior for the lower compared to higher velocities. These two regions of velocity could be found by looking at the angle between the flow and model. As *L. saccharina* has been shown to have near neutral buoyancy in water(Vettori, 2016), it is likely to behave as a 'tensile' plant even at lower velocities, unlike the models tested.

From the findings in this master thesis, future development of an artificial seaweed model for use as a surrogate of *L. saccharina*, should focus on models with undulate shape. Furthermore, to ease comparison with the hydrodynamic properties of the real seaweed, models should have the least amount of distorted parameters as possible. This to help uncover which parameters can be removed, and which are needed to correctly replicate important aspects of the seaweed hydrodynamics. In addition to looking at drag force, how the model influences the flow structure compared to the real seaweed should be examined. The reason for this being that oxygen and nutrient uptake are important factors to consider when optimizing seaweed farming.

Sammendrag

De siste årene har interessen for å dyrke og høste tare på et industrielt og kommersielt nivå i Norge økt. Ved å se på de hydrodynamiske egenskapene til tarefarmer, kan designet optimaliseres og dermed også mengden produsert biomasse optimaliseres. Dessverre er det ikke rett frem å bruke tare i eksperimenter. Blant annet har det blitt vist at det biologiske materialet til tare lett forringes når det blir utsatt for andre forhold enn de som er i miljøet det høstes fra. I tillegg er det mange eksperimentelle fasiliteter som ikke tillater at man introduserer biologisk materiale. Derfor er det nødvendig å designe kunstig tare som presist reproduserer de viktigste biomekaniske og hydrodynamiske egenskapene til ekte tare, for å kunne evaluere de hydrodynamiske egenskapene til tarefarmer. Det er viktig at egenskapene til taren på både blad- og koloninivå blir reprodusert.

Formålet med denne masteren, var å tilføre ny kunnskap om hydrodynamikken til tare, nærmere bestemt *Laminaria saccharina*, også kjent som sukkertare, til nytte for fremtidig evaluering av hydrodynamiske egenskaper til tarefarmer. Dette ble gjort ved å samligne dragkraft og oppførsel til to forenklede bladmorfologier, flat og bølget, begge med uniform tykkelse. Selv om tare blir utsatt for både havstrømninger og bølger, er oppførselen i bølger utenfor omfanget av denne masteroppgaven, og kun strømning ble vurdert. Forsøkene ble utført i det Marinkybernetisk laboratoriet til Institutt for Marin Teknikk ved NTNU. Laboratoriet har utstyr som tillater dragforsøk. To oppsett ble brukt, ett med kun en strømlinjeformet stang som gikk ned i vannet og ett med en sirkulær sylinder festet til den. Sylinderen var hul og hadde hull som tillot fargestoff å bli fordelt langs overflaten for visualisering av strømningen. Modellene ble festet nederst på oppsettet, og både blad- og koloninivå ble evaluert. To modellstørrelser ble testet for hver av de forenklede morfologiene. På grunn av høyt støyniva og vibrasjoner, ble rådata filtrert før gjennomsnittverdier og utviklingen av dragkreftene ble presentert. Opptak med undervannskamera tillot sammenligning mellom dragkraft og oppførselen til modellene mens de ble dratt gjennom vannet.

Hovedfunnet til denne masteroppgaven var, i motsetning til funnene gjort av Vettori (2016), at flate blader sannsynligvis ikke er gode surrogater for den bølgete taren *L. saccharina*. I samsvar med resultatene til Paul and Henry (2014), virker det sannsynlig at modellene oppfører seg an-

nerledes enn taren på grunn av forskjellig materialtetthet og dermed annerledes oppdrift. Det ble konkludert med dette etter å ha sett på videoopptakene ved lave hastigheter. Opptakene viste at modellene oppførte seg mer som tare som bøyer seg i respons til vannkrefter enn tare som er utstrekt i vannet ved disse hastighetene. I tillegg var det tydelig fra Vogel-eksponenten at modellene oppførte seg annerledes i respons til strømningen ved lave og høye hastigheter. Disse to områdene kunne bli gjenfunnet i videopptakene ved å se på vinkelen mellom vannbevegelsen og modellen. Siden *L. saccharina* har tilnærmet nøytral oppdrift i vann(Vettori, 2016), er det sannsynlig at den vil være utstrekt i vannet med liten vinkel selv ved lave hastigheter. I motsetning, hadde modellene en relativt stor vinkel.

Funnene i denne masteroppgaven tyder på at fremtidig utvikling av kunstige *L. saccharina*-taremodeller burde fokusere på bølgete modeller. Dessuten burde så få parametre som mulig avvike fra den ekte taren. Dette for å gjøre det lettere å avdekke hvilke parametere som kan ekskluderes og hvilke som er viktige, og trengs for å reprodusere de hydrodynamiske egenskapene til taren. I tillegg til å se på dragkrefter, burde fluidbevegelsene rundt taren og modellen undersøkes. Grunnen til dette, er at oksygen- og næringsopptaket til taren er viktige faktorer som må vurderes om man ønsker å optimalisere biomasseproduksjonen til tarefarmer.

Contents

Chapter 1

Introduction

1.1 Background

In recent years the prospect of having a seaweed based industry in Norway has become of interest. Seaweeds are widely used as a food source (mainly in Asian countries such as China, Japan and South Korea), as ingredients in cosmetics and fertilizers, and in hydrocolloid production (Chan et al., 2006; FAO, 2016). Seaweeds can also help make the aquaculture industry more sustainable through integrated multi-trophic aquaculture (IMTA) (Chan et al., 2006; Wang et al., 2012). In IMTA the waste from the fish is used as feed for organisms of lower tropic levels, such as mussels and seaweeds, cultivated in proximity of the fish farm. Among seaweeds, macroalgae such as kelps, are some of the fastest growing plants in the world, and occupy the lowest tropic level (Skjermo et al., 2014). With a world population of 7.3 billion in 2015, and a projected world population of 9.7 billion by 2050, sustainable food production will likely be a major challenge in the future (United Nation, Department of Economic and Social Affairs, Population Division, 2015). Currently, only 2 percent of the food energy comes directly from the sea, and seaweed is one of the largest unexploited global biomass resources (Skjermo et al., 2014).

The interactions deformable shapes, such as seaweeds, have with the surrounding flow is not well understood, as they exert force on the fluid through a coupling of their inertial and elastic responses (Zhang et al., 2000). *Laminaria saccharina*, the sugar kelp, is one of the species of interest for the Norwegian seaweed industry (Skjermo et al., 2014). The blades of this kelp have a complex undulate shape, with thickness decreasing in both longitudinal and lateral direction.

The effect of its morphological features on drag force, as well as its hydrodynamic response in general, is likely to be important when assessing the seaweeds hydrodynamic properties. However, seaweeds are difficult to care for and if harvested from nature, the experiments can only be conducted at certain periods during the year. Additionally, facilities such as flume tanks and towing tanks often do not allow biological material to be introduced. Artificial seaweeds, as surrogates that are able to replicate the hydrodynamic properties of seaweeds, are therefore of interest. Moreover, with the density being measured to be a few hundred plants per meter rope, by the author, there should be a focus on finding good surrogates that allow for quick and cheap mass production. To correctly assess the hydrodynamics of seaweed farms, relevant mechanism at the lower scales, i.e. blade and patch scale, should be isolated to allow for simplifications of the real system's complexity (Vettori, 2016). Relevant mechanisms at these lower scales must be maintained in the surrogates, to ensure that the hydrodynamic properties of the seaweed farm as a whole is correct.

1.2 Objectives

The main objective of this master thesis was to add to the knowledge about the hydrodynamics of the kelp *L. saccharina* for future assessment of the hydrodynamic properties of seaweed farms. This was done by:

- Giving a literature review of biomechanics and hydrodynamics of macroaglae, plant-fluid as well as plant-plant interactions, similarity theory and use of surrogates in previous studies.
- Performing, presenting and discussing results from blade and patch scale experiments of two models with a simplified morphology of *L. saccharina* at two different sizes.

For the literature review some main sources were used as starting points. The field of study regarding the biomechanics and hydrodynamics of macroalgae is relatively small. Starting off with well known works regarding hydrodynamics of aquatic ecosystems, such as Nikora (2010), helped introduce the author to this field of study, and also made her acquainted with earlier works and the history of the field. The PhD of Vettori (2016) was an experimental study that

looked at the hydrodynamic performance of seaweed farms, and was a good tool for finding information and sources more relevant to this master thesis focus on the kelp *L. saccharina*. Recommendations by the lecture notes from the class 'Experimental methods in hydrodynamics' (Steen, 2014) were used as a starting point to find good resources on modeling laws, dimensional analysis and similitude laws.

1.3 Scope and Limitations

The drag tests were performed at the Marine Cybernetics laboratory. During the runs, position, speed, acceleration and drag force were measured focusing on the stationary parts of the run. The position, speed and acceleration are for the carriage itself and not the models. There were no measurements of the velocity profile seen by the models, and no measurement of the fluid motion afterwards. So there is no information regarding how the models presence influence the flow. Even so, for the simple setup only a profiled cylinder influences the incoming flow and it therefore seems to be a fair assumption that the velocity of the incoming flow, as seen by the model, is approximately the same as the velocity of the carriage. However, this is not the case for the cylinder setup. With the exception of 20.5 [cm/s] run for the cylinder setup, the flow was not visualized. But, the behavior of the models when dragged, was recorded via an underwater camera. In conclusion, the focus of this master thesis is the mean drag force, in addition to using visual behavior to help propose possible mechanism for the tendencies and developments seen for the mean drag force.

The experimental facilities introduced limitations such as choice of fluid properties and possible velocities for the runs. The lower salinity of the water in the tank also meant that real kelp could not be tested and compared directly to the models. The reason being that it is likely that its biomechanical properties will change when it is exposed to the low salinity water (Vettori, 2016). Due to limitations in material choices for the surrogate, soft PVC was used. PVC does not have the same mechanical properties as the kelp tissue, with both higher bending modulus and density. Additionally, the models were made out of PVC sheet of uniform thickness. The heat treatment and subsequent manipulation to create the undulate shape for the undulate surrogates does introduce some reduction in thickness. Still, both the surrogates can be considered

to be uniform in thickness compared to the real kelp blade, where thickness varies both with its length and towards the sides. Due to the mechanical properties and morphology of the models being different from the real kelp, assessing of how well they perform as surrogates is difficult, but will be discussed. Even so, comparison of the two model morphologies and sizes is possible. The experiments look at both blade and patch scale, but does not look at different densities of the patches.

The experiments in this master thesis only look at the effect unidirectional flow has on the drag force and behavior of the models, excluding wave action. One of the reasons for this choice, is that the incorporation of wave action complicates the setup needed to record the response in an appropriate manner. If wave action is considered, then it will be beneficial to make a setup that can follow the wave motion as a rope would in a seaweed farm.

Chapter 2

Literature Review

This chapter contains a literature review on the morphological features of *Laminaria saccharina*, biomechanical properties and hydrodynamics of macroalgae, similarity theory for use in laboratory experiments and the design of surrogates used in previous studies.

2.1 Morphological Features of *Laminaria saccharina*

L. saccharina, also known as sugar kelp, is a macroalga. One plant consists of a holdfast, stipe and blade, see Figure 2.1. The stipe has a circular cross section that decreases in radius from the holdfast to the blade. The thickness of the blade decreases both longitudinal from the stipe and if one moves outwards towards the sides. The blade is not flat, but rather an undulate shape with ridges in the middle. The blade flattens towards the tip. This is not visible from the figure, as the tip has been removed, probably due to mechanical damage. Morphology and growth of *L. saccharina* has been studied to a certain extent, with examples being Parke (1948), Buck and Buchholz (2005) and Spurkland and Iken (2012).

Figure 2.1: Foto of *L. saccharina*. Photo taken by Jorunn Skjermo, SINTEF Ocean.

Studies have found that kelp plants collected from sheltered habitats are relative wide and often exhibit ruffles or undulate shape, while kelp collected from wave-exposed sites were longer and narrower, e.g. Koehl and Alberte (1988), Koehl (1999) and Buck and Buchholz (2005). Through his experiments where he applied mechanical stress to laboratory-grown *L. saccharina*, Gerard (1987) found that the plants that were subject to constant longitudinal tension had narrower blades and grew longer faster. The biomass-production rates, however, remained similar. He therefore concluded that mechanical stress through the environment could influence the morphology. Mechanical stress seems to influence morphology and elongation by affecting the orientation of cell division, not the cell size or rate of division. The blades becoming narrow due to longitudinal tension, this should reduce the drag from currents and waves, resulting in hydrodynamic streamlining. He also found that hydrodynamic streamlining did not affect the surface-to-volume ratio, meaning that it does not reduce the plant's capacity for photosynthesis or nutrient uptake. For *L. saccharina*, depending on the area where the plants are harvested, there are large variations in morphology Vettori (2016).

2.2 Biomechanical and Material Properties of Macroalgae

The reactions of an organism to the physical forces from a fluid flow is largely dependent on its biomechanical properties. In plant biomechanics, the traditional mechanics meet the diversity and complexity of biological systems. Biomechanics are specie specific, but there are some common features. According to engineering terminology, plants can be described as composite, anisotropic, viscoelastic, highly heterogeneous materials. (Nikora, 2010)

Viscoelastic materials do not possess a unique elastic modulus, instead the property is related to the time of which the load is applied (Wainwright, 1976). Compared to a linearly, elastic solid, a viscoelastic solid can absorb more energy per unit volume, but some of this energy is dissipated by processes such as creep and stress relaxation (Wainwright, 1976). Figure 2.2 contains plots of the stress as a function of extension ratio for the macroagla *Nereocystis leutkana*. This stress-strain behavior is characteristic for viscoelastic materials. The stippled area of the figure represents the work per volume required to pull the specimen (W_{pull}) and the hatched area represent the work per volume used for elastic recoil (W_{recoil}). The difference between these two

areas is the energy lost.

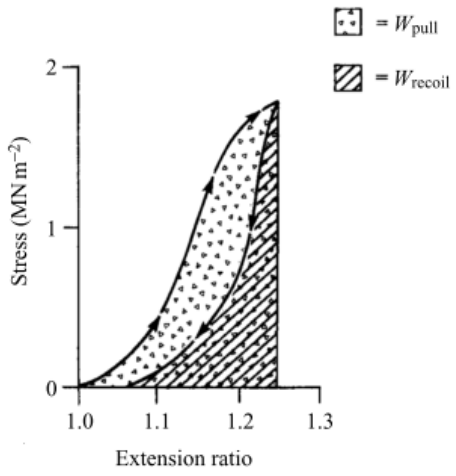

Figure 2.2: Stress-to-extention ratio of *N.luetkeana*. Adapted from Johnson and Koehl (1994).

While there are studies on the morphology of *L. saccharina*, knowledge on its biomechanics have been lacking. Vettori (2016) performed tests to look at the mechanical properties of the sugar kelp. The author performed similar tests during her summer at SINTEF Ocean. Table 2.1 contains the bending and elastic moduli as well as density of the blade of *L. saccharina* found from the two studies of the biomechanics of the *L. saccharina*. Vettori (2016) used force-displacement data from more than 120 tensile tests to find the elastic modulus and Pierce's method for evaluating the bending modulus with a sample size of 30. The author used tension test and Heart loop method(Pierce, 1930) to assess the elastic and bending moduli respectively with a sample size of 34 for both. As can be seen from the table, there is a large discrepancy in the elastic moduli found. This could be due to the apparatus used by the author for the tension test, as the apparatus was very primitive. The author chose to use Hearth loop method rather than Pierce's method, as there was some difficulties performing Pierce's method due to the undulate shape of the kelp blade. Simple test co compare the two methods have shown similar results. But the Heart loop method seems to be very sensitive to the accuracy of the weight measurements.

Table 2.1: Mechanical properties of the blade of *L. saccharina*.

Elastic modulus [MPa]	Bending modulus [MPa]	Density [kg/m^3]	Source
4.7 ± 1.8	3.7 ± 2.7	1092 ± 91	Vettori (2016)
1.0 ± 0.5	3.36 ± 1.32	1120 ± 130	Measurement done by author

Vettori (2016) found indications that the seaweed blades became stiffer as they grew. His results showed that longer seaweed blades were made of a stiffer and tougher material. However, the mean values of the elastic modulus were close to each other, indicating that the seaweed material is quasi-homogeneous. In an earlier study, Krumhansl et al. (2015) found that the breaking strain of kelp descreased while the initinal and final modulus increased significantly with distance from the base of the blade, thus making older tissue less flexible and extensible. The author herself was not able to find such a trend. This could be due to small sample size of small seaweed plants. Vettori (2016) also looked at the effect freshwater exposure has on seaweed biomechanics. He found that both elastic and bending moduli decreased with increasing time of freshwater exposure.

2.3 Flexural and Torsional Rigidity

Due to current and wave action the kelp will bend, or reconfigure, to reduce drag. Flexural rigidity J in a plant represents its ability to withstand the flow, and is important for determining to mechanical response of the plant. Flexural rigidity is defined as

$$J = E_b I \tag{2.1}$$

where E_b is the bending modulus and I the second moment of area of the cross section (Henry, 2014). E_b is an intrinsic value of the material, while I depends on the cross-section shape. For a circular cross section I is

$$I = \frac{1}{4}\pi r^4 \tag{2.2}$$

where r is the radius, and for a rectangular cross section it is

$$I = \frac{1}{12} b t^3 \tag{2.3}$$

where b is the breadth and t is the thickness, or

$$I = \frac{1}{12} b^3 t \tag{2.4}$$

depending on the direction of the bend (Wainwright, 1976). It can be seen that it is much easier to bend a thin, rectangular cross section over its thickness than its breadth.

The kelp plant does not only experience bending and stretching due to the drag forces, it can also experience torsion due to an applied torque, T_a. The following information is taken from Ugural and Fenster (2011). The angle of twist per unit length can be expressed as

$$\theta = \frac{T_a}{GI} \tag{2.5}$$

where G is the modulus of elasticity in shear and I is the polar second moment of area. The product GI is called the torsional rigidity of the member, expressing how easily the member can be twisted. As it is twisting instead of bending, the second moment of area is polar and defined somewhat differently. For a circular cross section it is

$$I = \frac{1}{2} \pi r^4 \tag{2.6}$$

and for rectangular cross section it can approximated as

$$I \approx \frac{1}{3} b t^3 \tag{2.7}$$

if $t \ll b$. This is the case for the blade of *L. saccharina*.

2.4 Hydrodynamics of Seaweed

Plants such as *L. saccharina* live in an environment that exposes them to both current and wave action. The strength of these parameters will depend on the location, i.e. sheltered vs. exposed. If the plants live in an environment with a current, but negligible wave action, the force experience by the plant would be almost solely due to the flow velocity of the current. The presence of waves however, causes the flow to accelerate and decelerate. Therefore, the total force experienced by the plants will be due to both the flow velocity and flow acceleration, i.e. drag force and hydrodynamic acceleration force respectively. Nonetheless, Gaylord (2000) found that fluid acceleration was negligible for the drag experience by marine organism such as kelp. The results from this experiment could be due to a lack of large fluid acceleration during the experiments, canceling-out effects or an intrinsic ability of the organism itself making it not experience hydrodynamic acceleration loads. However, in a later study it showed that this might only be true for organisms that bear forces in bending (Gaylord et al., 2001). For tensile organisms a very brief load was found to typically be doubled compared to what would have been expected for a static organisms. It is important to mention that the study used simplified shapes that might not represent the complicated morphology of intertidal plants.

Due to wave action being outside of the scope of the master thesis, this section will not concern the effects waves might introduce in the plant-fluid interaction problem. Instead the focus is the forces experiences by a plant in unidirectional flow, with special emphasis on drag force. This section will look at plant-fluid forces on blade scale level, as well as plant-plant interactions and their possible effects on drag force on patch scale, i.e. looking at multiple blades together and their interactions.

2.4.1 Plant-Fluid Forces and Interactions

Nikora (2010) presents an approximation of the forces due to plant-fluid interactions as three sets; fluid-induces, plant-induced and plant-reaction forces. The flow induced forces are the drag force

$$F_D = \frac{1}{2}\rho C_D A U^2 \tag{2.8}$$

and the lift force

$$F_L = \frac{1}{2}\rho C_L A U^2 \tag{2.9}$$

where ρ is the fluid density, and C_D and C_L are the drag and lift coefficient respectively, A the characteristic area, and U the relative velocity to the fluid. Plant-induced forces are the buoyancy force

$$F_B = \rho g V_p \tag{2.10}$$

and the gravity force

$$F_G = \rho_p g V_p \tag{2.11}$$

where g is the gravity acceleration, V_p the plant volume and ρ_p the plant density. Lastly, plant-reaction forces are the tensile reaction force

$$F_T = E\epsilon\omega \tag{2.12}$$

and the bending reaction force

$$F_b = \frac{E_b I}{Rx} \tag{2.13}$$

where ϵ is the strain, ω plant cross-sectional area, R radius of curvature at a point where a bending force is defined and x is the distance from the holdfast to the point where the resultant fluid force acts.

Several useful similarity numbers can be deduced by considering ratios of the aforementioned forces. One of them is the ratio between drag and bending force μ_{D-b}

$$\mu_{D-b} = \frac{F_D}{F_b} = C_D \frac{\rho U^2}{E}\left(\frac{L}{t}\right)^3 \tag{2.14}$$

that can be used to distinguish between 'tensile' and 'bending' plants, see Figure 2.3. A large μ_{D-b} number means that the drag force is dominant, and the plant can be characterized as a 'tensile' plant. While a small number signifies that the bending reaction force is dominant, and the plant a 'bending' plant. The relation $\rho U^2/E$ is known as the Cauchy number, Ca and $\rho U^2 L^3/Et^3$ a proposed way of describing the Cauchy number for flexible, thin objects as the original description of the Caucy number does not account for the morphology of the plant

(de Langre, 2008; Nikora, 2010). L is the length of the blade and t the thickness.

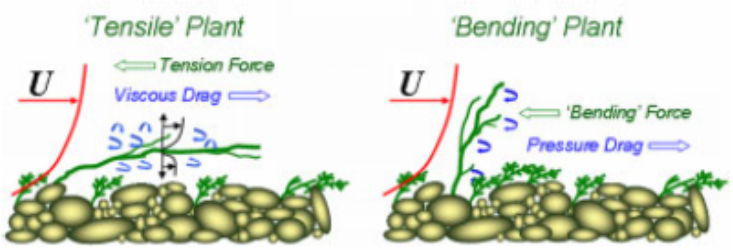

Figure 2.3: The two extremes: 'Tensile' and 'Bending' plant. Taken from Nikora (2010).

Due to its low flexural rigidity, the 'tensile' plant will reconfigure in response to the plant-fluid interactions and therefore experience mainly viscous drag. The 'bending' plant, on the other hand, has high flexural rigidity and the plant resists reconfiguration creating downstream vortices and separation with associated pressure drag. The plants needs to minimize the total drag while having sufficient mass-transfer and photosynthesis. Total drag can be minimized by minimizing plant surface area, thereby minimizing viscous drag, or by making the plant flexible and streamlined, reducing flow separation and therefore pressure drag.

The sugar kelp blade has very low flexural rigidity, causing the plant to passively follow the flow. This, in addition to having close to neutral buoyancy in sea weater means that it is best described as a 'tensile' plant and experiences mainly viscous drag. The stipe has a higher flexural rigidity, and bending of it likely cause pressure drag behind the stipe. Even so, it is a much smaller part of the plant, and the main contributor to the total drag is likely to be the blade viscous drag.

2.4.2 Parameterization of Drag Force

Drag Coefficient of Macroalgae

Drag parameterizations choices will affect the description of the drag coefficient and Reynolds number, as discussed by Statzner et al. (2006). The consequence of this being that researchers can obtain different drag coefficient and Reynolds number even when using the same experimental data, making direct comparison of results difficult. Looking at their definitions:

$$C_D = \frac{F_D}{\frac{1}{2}\rho A U^2} \tag{2.15}$$

$$Re = \frac{UL}{\nu} \tag{2.16}$$

it is A the characteristic area, U velocity and L characteristic length that must be chosen. Figure 2.4 shows three approaches and how they influence the drag force development for the same data. The dynamic manner, defines the characteristic area to be the frontal projection, causing the characteristic area to change when the plant reconfigure. On the other end of the spectra is the most static approach, which is defining the characteristic area as the total wetted surface area of the plant. The wetted surface area is constant, and therefore does not capture the dynamics of the fluid-plant interactions. This causes the drag coefficient to decrease with increasing Reynolds number, $C_D = f(Re) \propto Re^a$ where $a < 0$. An intermediate approach is using a lateral projected area where one parameter remains the same while the other changes with reconfiguration, similarly to frontal projection. An example of the two parameters are maximum horizontal diameter of the plant in still water and flow-dependent vertical plant height. For both the frontal and lateral projection, the drag coefficient increases with increasing Reynolds number, i.e. $a > 0$.

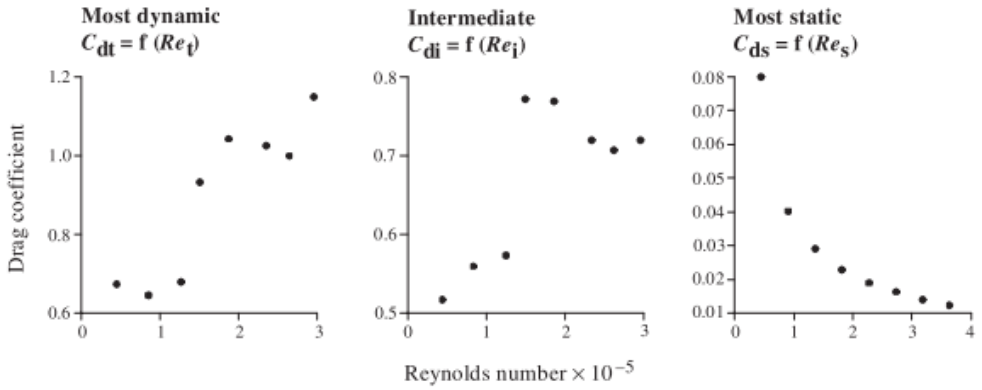

Figure 2.4: Plots showing how the drag coefficient develops with Reynolds number for *Egeria densa* in a boundary layer flow with three different approaches; frontal projection, lateral projection and wetted surface . Taken from Statzner et al. (2006).

The static approach is often used, and sometimes for blades their projected area, rather than wetted surface area, is the choice for the characteristic area. This causes the drag coefficient to

have the same trend, but to have a very different magnitude. This can be seen by comparing the most static approach in the previous figure with Figure 2.5. The figure also shows how a cluster of leaves will have a smaller drag coefficient than a single leaf, and how a blade can reconfigure to the flow. The reason the cluster of leaves has a smaller drag coefficient is due to self-shading within the group. A phenomenon that will be discussed in more details in Section 2.4.4.

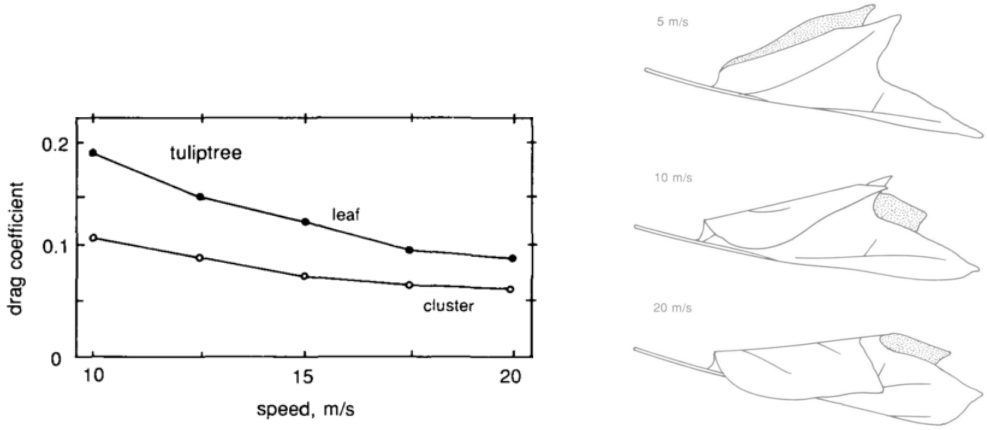

(a) Drag coefficient of tuliptree leaf and cluster with projected area in still air as characteristic area.

(b) Reconfiguration of tuliptree leaf traced from photographs at three different wind speeds.

Figure 2.5: Drag coefficient and reconfiguration of tuliptree. Taken from Vogel (1983).

Vogel exponent

The Vogel exponent is another method that can be used to parametrize drag and that looks at the efficiency of reconfiguration in a quantitative manner. While the drag coefficient denotes the drag relative to the fluid velocity and leaf area, Vogel exponent reflects how the drag coefficient varies with the fluid velocity (Vogel, 1989). For a blunt object that does not reconfigure in response to the flow

$$F_D \propto U^2 \tag{2.17}$$

is often used to describe the relation between drag force and velocity of the fluid. Even for an object fulfilling the requirements above, the relation is only true for a limited range of velocities and sizes (Vogel, 1984).

Biological organisms, such as macroalgae, are flexible and will reconfigure in response to an incoming fluid. The drag force is therefore expected not to follow the relationship seen in

Equation (2.17). Vogel (1984) proposed the relationship

$$\frac{F_D}{U^2} \propto U^{\psi} \tag{2.18}$$

where ψ is the Vogel exponent. By measuring the drag force at different velocities and plotting F_D/U^2 (ordinate) vs. U (abscissa), deviations from the horizontal line indicate that some form of drag reduction process, e.g. reconfiguration, has occurred. The Vogel exponent ψ can be found by performing a linear regression of the logarithms of F_D/U^2 and U. The slope is then ψ. For rigid, blunt bodies $\psi \approx 0$ and for flexible objects $\psi < 0$. The drag force experienced by a flexible object can then be expressed as

$$F_D = \frac{1}{2} C_D \rho A U^{2+\psi} \tag{2.19}$$

where the drag coefficient is assumed to be constant. The more negative the Vogel exponent is, the smaller increase of drag force with increasing velocity. Harder et al. (2004) found that the Vogel exponent was more negative for the brown seaweed *Durvillaea antarctica* taken from wave-exposed sides compared to sheltered, with $\psi = -1.00$ and $\psi = -0.73$ respectively, see Figure 2.6. Similar to *L. saccharina*, *D. antarctica* blades from sheltered areas are broad and have undulations. The blades from the wave-exposed areas however, are subdivided into many thin strips. The figure also shows how different velocity ranges can give different Vogel exponents with the giant reed *Arundo donax* as the example.

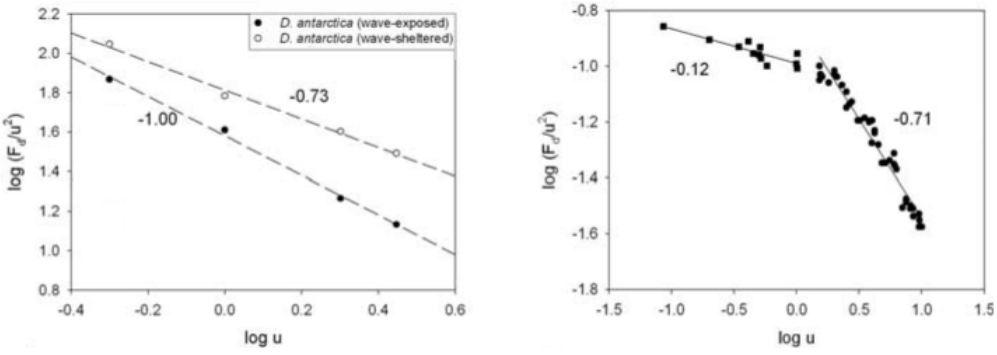

Figure 2.6: The Vogel exponent found for wave-exposed and sheltered *D. antarctica* and the Vogel exponent of *A. donax* for the wind velocities 0 to 1 [m/s] and above 1.5 [m/s]. Taken from Harder et al. (2004).

2.4.3 Parameters that Affect Drag Force on Blade Scale

There are a number of parameters that will affect the drag force on blades scale. The most important known parameters and how they affect the drag force will be discussed in the coming paragraphs.

Flexibility

The effect of flexibility has previously been mentioned. Flexibility allows the plant to reconfigure in response to the flow, thereby reducing drag. It has been found that the blade flexural rigidity is the more important than blade morphology and roughness (Albayrak et al., 2012). However, even if reconfiguration leads to reduced drag, studies have shown that drag coefficients of flags are considerably larger than the drag expected from skin friction drag along both sides (Hoerner, 1965). That is, the drag force experienced by the flexible flag is larger than that by a solid, stiff body of the same size. This has been shown to be due to additional pressure drag arising from fluttering of the flag, causing separation. The drag coefficient was found to be 10 times larger than the frictional drag estimated. Therefore, for a blade the flexibility might lead to increased drag if the blade becomes unstable in the flow and fluttering occurs.

Morphology

Morphology has been shown to affect drag force due to features such as serration (Albayrak et al., 2012), ruffles or undulate shape, and riblets. Albayrak et al. (2012) found that the leaf shape was not an important factor in determining hydrodynamic interactions. Additionally, *L. saccharina* does not have a serrated edge, therefore this aspect will not be considered further. It does however, have an undulate shape on the outer part of the blade, and it has been shown that undulate blades experience higher drag compared to flat blades (Buck and Buchholz, 2005; Koehl and Alberte, 1988). As can be seen from Figure 2.7, the undulation causes vortices and volumes recirculation. On the other hand, corrugations or riblets along the blade have been shown to causes reduction in drag force even though they increase the wetted surface area (Tani, 1988; Fryer et al., 2015). The reason for the undulation causing drag augmentation while corrugation and ribles cause reduction when both cause increased wetted area seems to be due to size and

distance (Djenidi et al., 1994). For undulation with diameters larger than the average diameter of the vortices, the vortices are found inside of the valleys. For small diameter valleys, such as those of riblets, the vortices lie mainly above. This causes only riblet tips to be exposed to skin friction, thereby reducing drag (Djenidi et al., 1994).

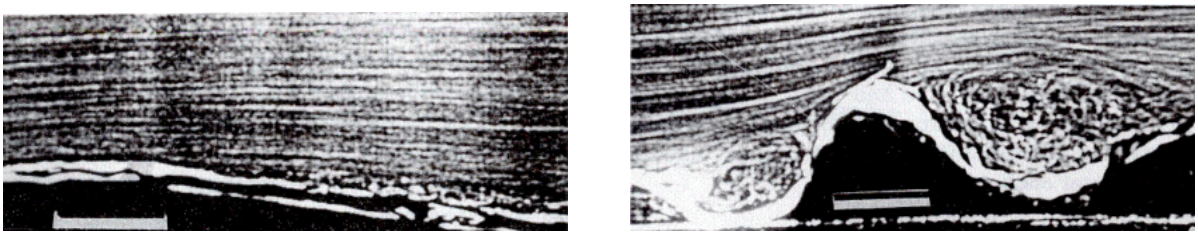

(a) Flat blade from exposed area. (b) Undulate blade from sheltered area.

Figure 2.7: Streaklines of the flow over blades of *Macrocystis integrifolia* at 8 [cm/s]. Scale bars on both pictures are 1 [cm]. Taken from Hurd et al. (1997).

Material Properties

Paul and Henry (2014) found that identically shaped surrogates of different materials lead to different velocity and turbulence profiles. The study confirmed that how flexible structures streamline under hydrodynamic forcing depends on the materials buoyancy and stiffness. Their observations make sense when considering the approximations of plant-fluid interaction forces proposed by Nikora (2010), see Section 2.4.1. The gravity force depends on the density of the plant, while the tensile and bending reaction forces depend on the elastic and bending modulus respectively. Difference in density will cause the model to be positioned differently in the fluid, while the elastic and bending properties will influence plant-fluid interaction such, as reconfiguration as discussed previously.

Roughness

Biofouling produces an increase in roughness of the surface. One form of biofouling can be seen in Figure 2.8. It can also be seen from the picture that it increases the thickness of the blade, thereby making it less flexible. The drag experienced by the kelp is therefore likely to increase as the kelp grows older and has more biofouling. Additionally, some studies have found that the kelp material becomes stiffer with age, see Section 2.2. The biofouling also makes the kelp more

brittle, and more prone to breaking as a result of mechanical damage. Albayrak et al. (2012) looked at three combinations of the surface roughness, both sides rough, one of each and both sides smooth, and found that surface roughness enhanced the drag force acting on the blade at high Reynolds numbers.

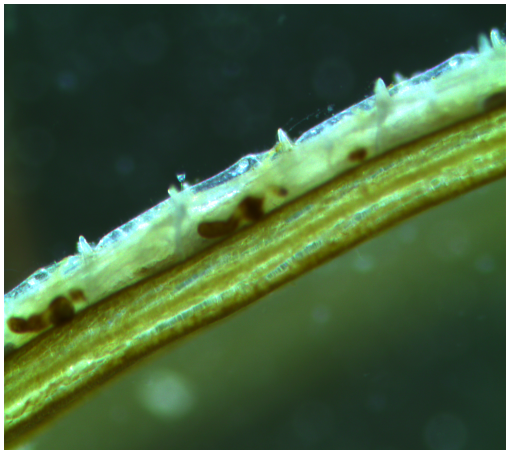

Figure 2.8: Stereo microscope picture of blade cross section with biofouling on top surface. Photo taken by Carina Norvik.

Aspect Ratio

Aspect ratio is the ratio of a geometrical shape's different dimensions, e.g. span to mean chord for wings. For a flag the aspect ratio can be defined as the ratio between the height and length, where the length is in the direction of the flow. Similarly, for a kelp blade it can be defined as

$$AR = w/L \tag{2.20}$$

where w is the width and L the length of the blade. Morris-Thomas and Steen (2009) looked at flexible sheets in uniform parallel flow in the Reynolds number range of $10^4 - 10^6$ and with varying aspect ratios between 0.43 and 1. During experiments that did not have in-plane tension, the flexible sheets resembled flags, and it was observed that the drag coefficient decreased with decreasing aspect ratio. The same tendency was found by Carruthers and Filippone (2005) when they looked at the aspect ratios 0.1, 0.05 and 0.03.

2.4.4 Patch Scale Interactions and the Effect on Drag

The majority of studies concerning plant-flow interactions of seaweed have looked at isolated plants, even though kelp such as *L. saccharina* are found in communities. This can be described as the patch scale (Vettori, 2016). One important parameter for describing a patch, is its density (Nikora, 2010). There are different manners of describing the density, e.g. plants per surface area. For *L. saccharina* grown on ropes in a seaweed farm, plants per meters rope might be the most natural way of describing the density. On this scale, both plant-plant interactions when placed in parallel and tandem are of interest and will be discussed with the focus being on how it influences behavior and drag force.

Interaction Between Parallel Blades

Luhar and Nepf (2011) found that the presence of neighboring blades can change the flow structure, thereby affecting the reconfiguration response. It is therefore important to recognize that the drag results from an experiment with a single macroalga, can not automatically be multiplied by the number of plants of interest and assumed to be a good approximation of the total drag. Different densities of plants in a patch will also yield variations in flow structure Luhar and Nepf (2011). Therefore, the same number of plants might not experience the same total drag force at different densities.

As previously discussed in Section 2.1 and 2.4.2, blades of kelp have been found to have different morphology and drag coefficient in different hydrodynamic environments. An undulate blade from protected habitats have been found to have higher drag coeffcient than the a narrower, flatter blade found in exposed areas. Johnson and Koehl (1994) looked at the giant kelp, *N. leutkeana*, where one plant consists multiple blades attached to a pneumatocyst, see Figure 2.9, thereby acting as a cluster on patch scale. Similarly to single blades, they found that at a given velocity the flatter blades from the exposed areas had a lower drag coefficient than the undulate blades. The reason being that the flatter blades flapped at a lower amplitude and collapsed together into a narrower bundle. It therefore seems that an undulate shape not only affects the drag force on blade scale but also on patch scale, influencing the plant-plant interactions.

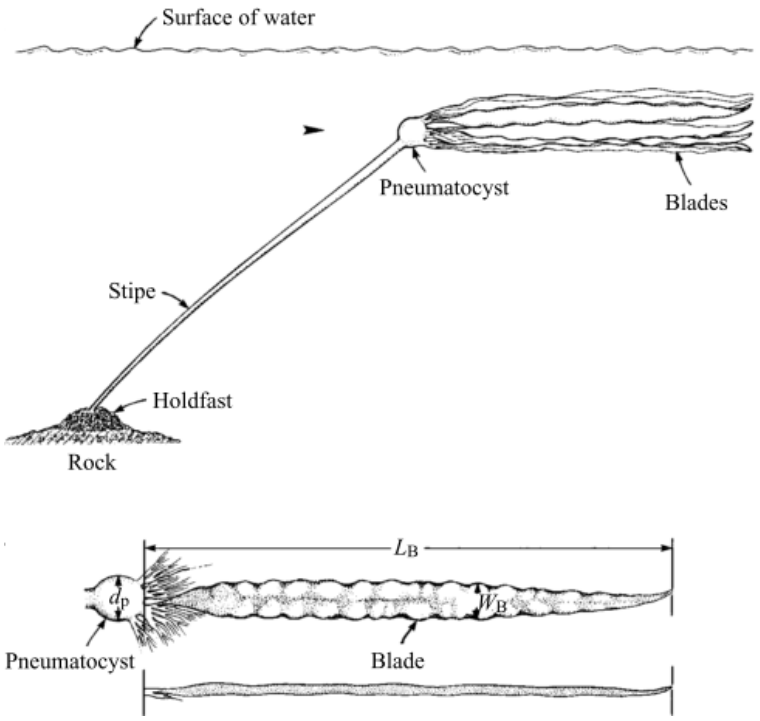

Figure 2.9: Morphological features of *N. luetkeana*. Taken from Johnson and Koehl (1994).

However, Vettori (2016) did not find evidence of interaction between the seaweed models in his investigation of seaweed models in parallel. This is in contrast to the findings of Zhu and Peskin (2003), Farnell et al. (2004) and Alben (2009). Both Zhu and Peskin (2003) and Farnell et al. (2004) found that flexible filaments osciallated in-phase or anti-phase depending on the separation between them, also referred to as parallel flapping and mirror-image clapping. Vettori (2016) noted that the reason for the lack of interaction appeared to be due to the experiments not allowing the models to oscillate in horizontal direction.

Interactions Between Tandem Blades

Rigid bodies behind a leader experience drag reduction in a flow (White, 2011). This effect is understood by considering that the downstream bodies sit in the wake of the leading body and therefore meet a lower fluid velocity. However, for flexible, changing bodies such as schooling fish, flapping flags and kelp, this might not be true. Ristroph and Zhang (2008) found that for flags in tandem, the leading flag of the group experienced up to 50 % reduction in drag while the downstream flags had an increase in drag force. They also found that when looking at a pair

in tandem, the pair as a whole can have a drag reduction or increase depending on the distance between them. Figure 2.10 shows how the drag force and fluttering amplitude of the flags are influenced by the relation of the gap between the flags and length of the flags.

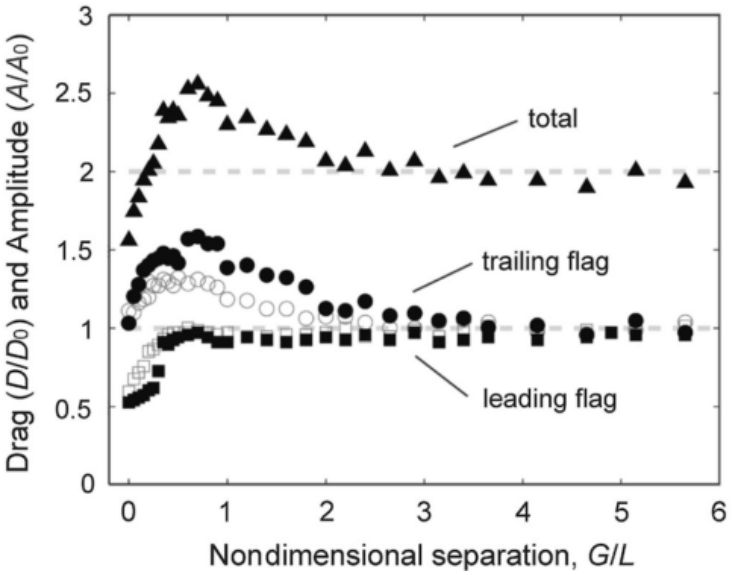

(a) Leading flag normalized drag (solid squares) and normalized flapping amplitude (open squares) are lower than for a single, isolated flag. Trailing flag normalized drag (solid circles) and normalized flapping amplitdue (open squares) are higher. Total drag of the pair (solid triangles) is reduced for small gaps and amplified for larger gaps compared to the total drag of two independent flags. The nondimensional separation, is the gap between the flags divided by the flag lengths.

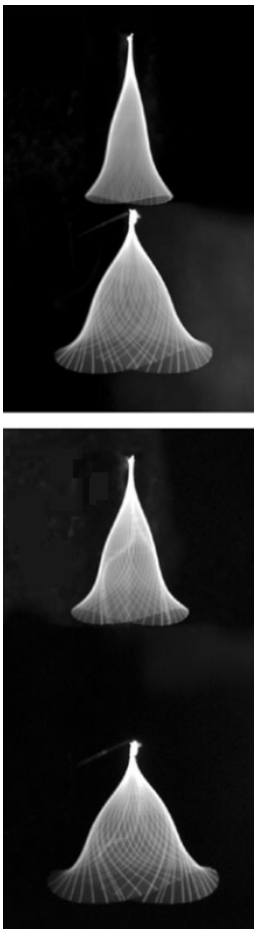

(b) Periodic motion captured by long-time exposure photographs.

Figure 2.10: Drag and flapping amplitude as well as total drag and two examples of periodic motion of two flags in tandem. Taken from Ristroph and Zhang (2008).

When Vettori (2016) looked at a pair of his seaweed models in tandem, he found the total drag to be independent of the longitudinal separation between them. The upstream model experienced a higher drag than the downstream model. This is in contrast with the findings in the previous study mentioned. Vettori (2016) theorized that his contradictory findings could be due to the models morphological characteristics or the hydraulic conditions during the experiment.

2.5 Design of Artificial Seaweed

This chapter concerns the design of artifical seaweed. As the models need to act similarly to the real kelp, similarity theory will first be introduced, before discussing the relative importance of different dimensionless number to the problem. Lastly, this chapter will look at previously used artificial seaweeds and the design choices made. Due to many of the previous studies use of scaled models, this chapter will also look into the theoretical background for scaling of the fluid phenomenom and plant-fluid interactions. The content of this chapter, if not otherwise specified, is based on Chakrabarti (1994), Steen (2014), Taylor (1974) and White (2011).

2.5.1 Similarity Theory

Complete similitude of model and full scale can only be obtained on 1:1 scale. Therefore, when scaling it is important to identify which parameters are significant and which can be omitted. Omitting parameters that have a significant impact on the problem at hand, can lead to erroneous results, while including too many can result in laws that become to complicated and even impossible to satisfy.

To be able to achieve similarity between the forces in full and model scale, it is required that they have geometric, kinematic and dynamic similarity. Geometric similarity, or similarity in form, entails that the length ratios in full and model scale are the same. That is, any given length in a model of 1:λ scale should satisfy the relation

$$L_M = \frac{1}{\lambda} L_F \tag{2.21}$$

where L_M is a length in model scale, L_F is the corresponding length in full scale, and λ is the scale parameter. Geometric similarity is also needed for the flow field and the environment, e.g. the distance to the sea bottom compared to the length of the model. Kinematic similarity, also known as similarity of motion, entails that the ratios between velocities and accelerations in full and model scale should be the same. Lastly, dynamic similarity is similarity in forces acting on the fluid. This is achieved if the ratios between forces are the same in both scales, in addition to elastic relative deformations being identical for elastic models. Other ratios of forced acting on a structure present in a flow field must also be equal for correct scaling, e.g. pressure,

gravity, viscosity and surface tension. If geometrical similarity is satisfied, dynamic similarity must be satisfied to get kinematic similarity. When scaling down from full size it might not be possible to scale all geometrical parameters correctly. Instead a distorted model can be used. However, it should be noted that distorting the geometry, will to some extent also distort velocity distributions and their effects.

When describing full-scale physical models in a smaller scale, the small scale should be able to describe the full scale physical system as close as possible. Dimensional analysis can be used to derive dimensionless quantities. Which of these are of significance and which can be omitted will depend on the problem at hand. White (2011) introduces dimensional analysis in Chapter 5, and describes it as a method for reducing the number of variables that affect a given physical problem. There are multiple methods for reducing the number of dimensional variables, one prominent example being *Buckingham Pi Theorem*, that was first proposed by Buckingham (1914). Before a dimensional analysis is performed, it must be know that there exist a relationship between a certain number of physical quantities, and that no relevant quantities are omitted. According to the *Buckingham Pi Theorem*, this relationship can be expressed as

$$\phi(q_1, q_2, q_3, ..., q_n) = 0 \tag{2.22}$$

where q_i is the numerical value of quantity i, and the problem has n important physical quantities. These quantities can then be regrouped to get dimensionless ratios Π_i,

$$\phi(\Pi_1, \Pi_2, \Pi_3, ..., \Pi_m) = 0 \tag{2.23}$$

where $m < n$. The dimensional analysis therefore eliminates extraneous information. Functional relationships can also be written so that one dependent dimensionless Π is a function of the other $m-1$ dimensionless quantities.

$$\Pi = \phi(\Pi_1, \Pi_2, \Pi_3, ..., \Pi_{m-1}) \tag{2.24}$$

Usually in fluid mechanical problems there is said to be four basic dimensions - mass M, length L, time T and temperature Θ. However, it is reasonable to assume that temperature will

have little effect when the fluid in question is water, and can therefore be omitted. This is due to water having very similar properties for the relevant temperature range. What remains is then a MLT system. It is of interest to know the values a, b and c for the quantities' dimensions described as $M^aL^bT^c$, see Table 2.2.

Table 2.2: Dimensions of some fluid-mechanical properties.

Parameter	Symbol	MLT system	Dimensions		
			a	b	c
Length	L	$\{L\}$	0	1	0
Area	A	$\{L^2\}$	0	2	0
Volume	V	$\{L^3\}$	0	3	0
Time	T	$\{T\}$	0	0	1
Velocity	U	$\{LT^{-1}\}$	0	1	-1
Mass	M	$\{M\}$	1	0	0
Force	F	$\{MLT^{-2}\}$	1	1	-2
Density	ρ	$\{ML^{-3}\}$	1	-3	0
Dynamic viscosity	μ	$\{ML^{-1}T^{-1}\}$	1	-1	-1
Kinematic viscosity	v	$\{L^2T^{-1}\}$	0	2	-1

In fluid mechanics common dimensional variables are geometry of the structure, fluid properties such as density and viscosity, and properties of fluid motion such as velocity and pressure. These parameters can be written as the relationship

$$\phi(L_1, L_2, U, p, \rho, \mu, \sigma, E, g) \tag{2.25}$$

that can be rewritten and made dimensionless to become

$$\phi(\frac{L_2}{L_1}, \frac{p}{\rho U^2}, \frac{\rho U L_1}{\mu}, \frac{U^2}{gL_1}, \frac{\rho U^2 L_1}{\sigma}, \frac{\rho U^2}{E}) \tag{2.26}$$

where the third, fourth, fifth and sixth dimensionless quantity is the Reynolds number, Froude number, Weber number and Cauchy number.

2.5.2 Evaluating the Relative Importance of Dimensionless Numbers

Some common dimensionless numbers in fluid flow problems can be found in Table 2.3. Dynamic similarity is achieved when these ratios are the same for model and prototype. Several ratios may be involved in scaling. However, often one of the ratios predominates.

Table 2.3: Some dimensionless numbers used in hydrodynamic scaling. Adapted from Chakrabarti (1994), White (2011) and Vettori (2016).

Dimensionless number	Ratio or physical process	Equation
Froude number	Inertia force / Gravity force	$Fr = \frac{U}{\sqrt{gL}}$
Reynolds number	Inertia force / Viscous force	$Re = \frac{UL}{\mu}$
Cauchy number	Inertia force / Elastic force	$Ca = \frac{\rho U^2 L^3}{Et^3}$
Strouhal number	Vortex shedding	$St = \frac{f_n L}{U}$
Keulegan-Carpenter number	Period parameter	$KC = \frac{U_A T_A}{L}$

When studying wave dynamics, Froude scaling is most extensively used for the models. For bodies that are in proximity of the surface, or penetrate it, interactions with the surface is considerable. The object creates a pressure field that cause a wave system to be generated. To correctly scale the wave system generated, Froude similiarity is needed (Hoerner, 1965). The Froude number considers the effect of gravity on the system, and the ratio of inertia force to the gravitational force. In problems considering water flow where free surface is pierced, the gravitational effect predominates.

Normally, the experimental facilities are not able to get the needed velocities for Reynold scaling. Problems often arise in achieving identical Reynold numbers for flying aircraft and ships in full and model scale (Hoerner, 1965). However, this might not be an issues for seaweed farms, as they most likely will be in quite secluded areas with relatively low current velocities. According to Reynolds' similarity law the flow patterns and drag coefficients of two bodies with identical shape, but different size, in the same or different fluid medium, are similar if the Reynold number is identical for the two bodies (Hoerner, 1965). If viscous effects are important, Reynold similarity is needed.

A dimensionless number not mention in the table above is Euler number. Euler number is rarely important, unless pressure drops so that cavitation will occurs. This is not a concern when

looking at a kelp plant in fluid flow. The Cauchy number on the other hand, will be important to reproduce in the small scale model when the prototype is elastic and experience bending, which is the case for macroalgae. Strouhal number is important if there is vortex shedding on the structure. Previous studies done by Huang et al. (2011) theorized that the flapping motion of the blade is a product of vortex shedding due to its undulate shape acting in a similar manner as cylinders. However, the results of their experiments did not support this theory. Keulegan-Carpenter number is important when having wave action and current action together.

For the kelp-water interaction problem the most important dimensionless numbers are Froude number and Reynolds number. Due to the streamlining of the long kelp blade, skin friction will be one of the main contributors to the drag force. Skin friction is a type of viscous force and having the same Reynolds number for model and full scale, will ensure that the skin friction is correctly scaled. Even so, many of the previous studies using scaled artificial kelp have chosen to use Froude similitude for scaling, see Dubi (1995) andRosman et al. (2010). They argued that the drag coefficient should be similar in full and model scale for the Froude number used. Vettori (2016) on the other han, kept the Reynold number identical for his *L. saccharina* models. As both Reynold and Froude similarity have been used by previous studies and are the two most important dimensionless numbers, the following sections shows how different parameters such as velocity and elastic modulus are effected by the two scaling laws.

Reynold Similarity

Equality in Reynolds number will ensure that the ratio of inertia to viscous force is correctly scaled. Reynolds similarity entails that

$$Re = \frac{U_M L_M}{\upsilon_M} = \frac{U_F L_F}{\upsilon_F} \tag{2.27}$$

where Re is the Reynolds number, U_M and U_F are the velocities of the fluid as seen by the kelp, and υ_M and υ_F the kinematic viscosities, with the subscripts M and F denoting model and full scale respectively. The Reynold similarity can be used to find the correct model scale velocity. From there, with the scale factor defining length, it is possible to find the scaled mass and time. The mass, time and length relationships can then be used to find the relationship between full

scale and model by using the *MLT* system. For simplicity, the ratios δ_ρ and δ_υ have been defined. δ_ρ is defined as ρ_{pF}/ρ_{pM}, the ratio of the model density in full and model scale. Similarly, δ_υ is defined as υ_F/υ_M, the ratio of the kinematic viscosity of the fluid in full and model scale. Table 2.4 contains some relevant Reynold similarities, as well as simplified similarities where $\delta_\rho = \delta_\upsilon = 1$. That is, the fluids' kinematic viscosities and the models' densities are the same for both scales. Stepwise deduction of the relationships can be found in Appendix A.

Table 2.4: Summary of Reynolds similarities.

Parameter	Basis	Relationship X_F/X_M	Simplified relationship
Length	$\lambda = L_F/L_M$	λ	λ
Velocity	$Re = \frac{UL}{\upsilon}$	$\delta_\upsilon \lambda^{-1}$	λ^{-1}
Mass	$M = \rho V$	$\delta_\rho \lambda^3$	λ^3
Time	$T = \frac{L}{U}$	$\delta_\upsilon^{-1}\lambda^2$	λ^2
Force	$[F] = MLT^{-2}$	$\delta_\rho \delta_\mu^2$	1
Elastic and bending modulus	$[E] = [E_b] = ML^{-1}T^{-2}$	$\delta_\rho \delta_\upsilon^2 \lambda^{-2}$	λ^{-2}
Moment of inertia	$[I] = L^4$	λ^4	λ^4
Flexural rigidity	$[J] = ML^3T^{-2}$	$\delta_\rho \delta_\upsilon^2 \lambda^2$	λ^2

Froude Similarity

Equality in Froude number will ensure that the ratio of inertia to gravity force is scaled correctly. Froude similitude entails that

$$Fr = \frac{U_M}{\sqrt{g_M L_M}} = \frac{U_F}{\sqrt{g_F L_F}} \tag{2.28}$$

where g_M and g_F is the gravitational acceleration in model and full scale respectively. As long as both experiments are conducted on Earth, these will be approximately the same with only slight variations due to the relative elevation and where on Earth the experiments are conducted. The relationship between model and full scale can thus be simplified to

$$\frac{U_M^2}{L_M} = \frac{U_F^2}{L_F} \tag{2.29}$$

Similarly to what was done previously for Reynold scaling, a number of parameters have been found for the full scale in relations to model scale, see Table 2.5. Stepwise deduction of the relationships can be found in Appendix B.

Table 2.5: Summary of Froude similarities.

Parameter	Basis	Relationship X_F/X_M	Simplified relationship
Length	$\lambda = L_F/L_M$	λ	λ
Velocity	$Fr = \frac{U}{\sqrt{gL}}$	$\lambda^{1/2}$	$\lambda^{1/2}$
Mass	$M = \rho V$	$\delta_\rho \lambda^3$	λ^3
Time	$T = \frac{L}{U}$	$\lambda^{1/2}$	$\lambda^{1/2}$
Force	$[F] = MLT^{-2}$	$\delta_\rho \lambda^3$	λ^3
Elastic and bending modulus	$[E] = [E_b] = ML^{-1}T^{-2}$	$\delta_\rho \lambda$	λ
Moment of inertia	$[I] = L^4$	λ^4	λ^4
Flexural rigidity	$[J] = ML^3T^{-2}$	$\delta_\rho \lambda^5$	λ^5

2.5.3 Surrogates From Previous Studies

In general surrogates, or artificial seaweeds, are used for experiments on vegetation-hydrodynamic interactions. Many facilities do not allow biological material and water with a salinity similar to seawater. If there is a lower concentration of ions in the water than in the plants natural habitat, there will be an osmotic pressure and water will enter the cells of the plant changing its biomechanics. However, as Johnson et al. (2014) points out, by simplifying aspects of the morphology, like surface texture, it is likely that the interaction between the flow and surrogate will be different from the interactions between the flow and the real plant. They also mentions that another limitation of using surrogates is that there is a possibility that an important, unknown impact of the organism on the interaction being studied is omitted.

Previous studies such as Ghisalberti and Nepf (2002), Paul et al. (2011) and Stratigaki et al. (2011) looked at seagrass models. Bouma et al. (2005) looked at models of the shoots of *Spartina angelica* and *Zosteria noltii*. Their resemblance is closer to the stem than the blade of the *L. saccharina*. Due to the blade being much larger than the stipe, it seems likely that the blade will be more important for *L. saccharina* surrogates.

The models used in Dubi (1995) doctoral dissertation were 1:10 Froude scaled. The model of a single kelp can be seen in Figure 2.11. As can be seen from the figure, the morphology of *L. hyperborea* was kept with no significant simplification.

(a) Kelp model (b) Kelp forest (Løvås and Tørum, 2001)

Figure 2.11: The model made by and experimental setup used by Dubi (1995).

Rosman et al. (2010) made 1:25 Froude scaled models of *M. pyrifera*. One *M. pyrifera* plant consists of one holdfast that has multiple stipes, and where along each stipe there are pneumatocysts, i.e. bladders. Each pneumatocyst has one blade attached. The kelp was modeled as an array of vertical cylinders, with or without the canopy, see Figure 2.12. Their reason for having a model with canopy was that during the summer and autumn most of the kelp biomass is in the surface canopy. A simple cylinder model of the kelp forest may therefore not give appropriate results. The frontal area (of the stipes) and buoyancy distribution were correctly scaled, however the dimension of individual components were not. As can be seen from the pictures, the blades that would normally be attached to the pneumatocysts are not present in the model.

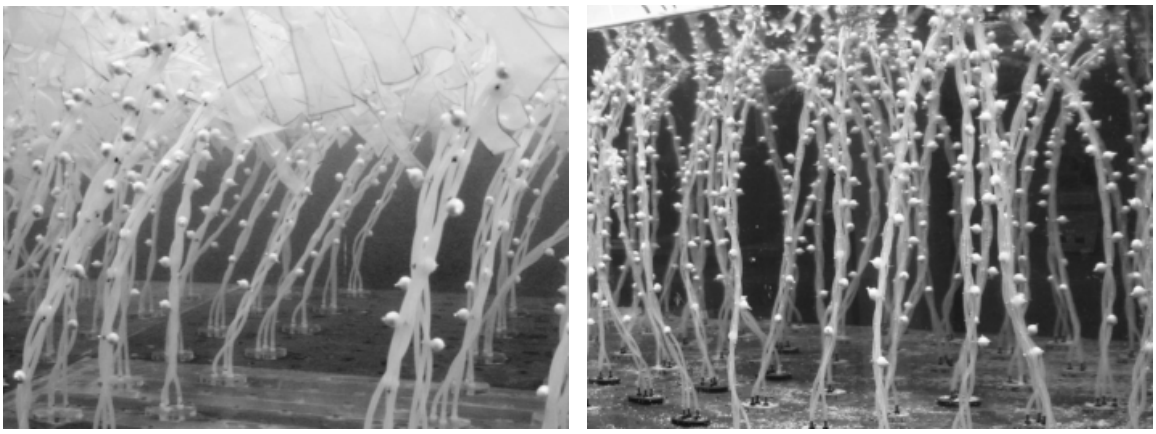

(a) With canopy (b) Without canopy

Figure 2.12: The model experiment setup of Rosman et al. (2010).

Vettori (2016) developed a similarity theory for seaweeds. The first step he took was selecting the relevant parameters at blade and patch scale, and used these parameters to create so-called governing dimensionless parameters. Similarly to this master thesis, his main focus was on the drag force, and used the simplification that waves and their effects on governing parameters could be neglected. He chose to use Reynold similarity when scaling, in contrast to the previous studies mentioned. However, he could consequently not keep the Froude number identical. The length of the seaweed model was the limiting factor and the experimental design was set to 1:5 for any dimension of the seaweed model. Seaweed samples of *L. saccharina* collected from a sheltered location in Scotland were used to design the models. The models did not have their macrofeatures, see Figure 2.13 which shows a seaweed with a model's contour in black superposed. The models were in general narrower than seaweed blades, with uniform width and no ruffles or irregularities. The models therefore had a lower surface area compared to equivalent seaweed blades. Additionally, how thickness varies along and across the seaweed blades was not replicated.

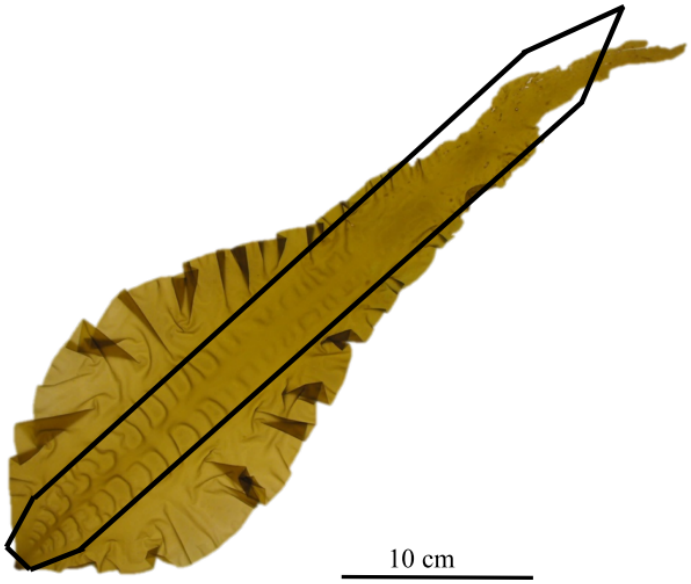

Figure 2.13: A seaweed blade and contour of a seaweed model by Vettori (2016).

The seaweed models were made by using polyethylene sheets with thickness between 0.07 and 0.27 [mm]. The material density of the models were 75 - 97 % of the real kelp and the elastic modulus 17 - 68 times larger, with the target being 25 times larger as to coincide with the set scale ratio of 1:25, meaning many had too high elastic modulus. However, this deviation did not seem to affect the results, as models with density and elastic modulus closer to the target values did not perform better. Vettori (2016) did a comparative analysis of seaweed blades and models, and found that biomechanical properties were not an important factor in the cases considered, i.e. high slenderness, high flexibility and high Reynolds number. Vettori (2016) found that the models successfully reproduced many aspects of the seaweed blade dynamics in spite of the difference in morphology, i.e. lack of undulation.

2.6 Knowledge Gaps

This chapter has examined what knowledge is available concerning the biomechanical and material properties of macroalgae, morphological features for the kelp of interest, *L. saccharina*, the hydrodynamics of seaweeds on both blade and patch scale, and previous use of surrogates in other studies. The field of biomechanics and hydrodynamics of macroalgae is quite small. Even so, in last ten years there has been a large increase in the number of publications within

this field (Henry, 2016). Many of the studies have focused on aquatic vegetation in rivers or the vegetations role in wave damping (Dubi, 1995; Rosman et al., 2007; Siniscalchi, 2012). These studies look at macroalgae that grow in the river or on sea bottom, and can often be classified as 'bending' plants. Among these studies, the ones using scaled models have only done simple comparisons of drag force for model and kelp to verify the validness of the surrogates, if any validation process has been performed at all. Some work have been done looking at how different parameters, such as density, shape and flexibility, influence the models, e.g. Paul and Henry (2014), Albayrak et al. (2012), Buck and Buchholz (2005) and Koehl and Alberte (1988). However, these have mainly been on blade scale and to correctly represent the seaweed farm hydrodynamics, patch scale must also be considered.

Until recently, the main focus when looking at the hydrodynamics of macroalgae, has been on bending organisms. However, in recent years with work such as the PhD *Hydrodynamic Performance of Seaweed Farms: an Experimental Study at Seaweed Blade Scale* of Vettori (2016) and this master thesis, there seems to be an emerging interest in the hydrodynamics of seaweeds to use on a commercial level in seaweed farming, thereby shifting some of the focus to 'tensile' rather than 'bending' macroalgae. To assess the hydrodynamics of seaweed farms, relevant mechanisms at blade and patch scale must be isolated and incorporated into the surrogates. Therefore, isolating and investigating how different parameters affect the hydrodynamic properties on the lower scale, is important. There have been done experiments looking at how a flat blade and undulate blade are in terms of drag and behavior, e.g. Johnson and Koehl (1994). The main findings have been that they behave differently on patch scale. However, in contrast to other studies, Vettori (2016) found that his flat models were good surrogates to the undulate *L. saccharina*. Therefore, further investigation into how the shape of the models affect its behavior is needed to ensure proper assessment of the hydrodynamic properties of seaweed farms. Additionally, as of now the knowledge about interaction of seaweed blades in tandem, mainly comes from studies looking at flags, or flexible filaments, in flow. These do not account for possible difference in behavior due to the more complicated morphology of kelps.

Some studies have found that hydrodynamic forces due to accelerations are negligible for marine organisms such as kelp (Gaylord, 2000). However, results from other studies suggest that 'tensile' and 'bending' plants react differently to brief loads, and that tensile organisms typically

experience a load doubled of what is expected for a static organism (Gaylord et al., 2001). If the findings of the later study are not only true for the simplified shapes investigated, but also for kelp such as *L. saccharina*, acceleration due to wave action could be a large contributor to total experienced drag force of the seaweed farm, and should be investigated.

Chapter 3

Methods and Materials

3.1 Surrogate Models

Two model sizes were used in these experiments, see Table 3.1. Both models were cut out of the flexible PVC material *Achilles Vinistar* by the supplier.

Table 3.1: Model parameters and ratios compared to the kelp *L. saccharina*.

Parameter	Small model	Large model
Total length [mm]	674	1035
Blade length [mm]	500	810
Blade maximum width [mm]	70	150
Stipe length [mm]	174	225
Stipe width [mm]	3.78 - 4.50	4.08 - 5.20
Model thickness [mm]	0.40	0.40
Projected area [mm^2]	25689	90641
Blade aspect ratio [-]	0.14	0.19
Bending modulus [MPa]	18.87	18.87
Ratio between the blade flexural rigidity of the model and kelp [-]	4.4	2.7
Ratio between the stipe flexural rigidity of the model and kelp [-]	$9.57 \cdot 10^{-5}$	$6.80 \cdot 10^{-5}$
Ratio between the stipe torsional rigidity of the model and kelp [-]	$1.91 \cdot 10^{-4}$	$1.35 \cdot 10^{-4}$

PVC does not have the same elastic or bending modulus as what have been found for sea-

weed, 18.87 [MPa] compared to 3.36 [MPa], when using the Heart loop method. To obtain the same flexural rigidity as the real plant, the thickness was reduced, see Equation (2.1). Unfortunately, it was not possible to obtain the thickness needed to get models of correct flexural rigidity by the time the laboratory was available. The models are therefore stiffer than the kelp, 4.4 and 2.7 times stiffer for the small and large model respectively. On the other hand, the torsional rigidity of the model stipe is less than 1/1000 and 1/10000 of the kelp stipe.

Half of the models were heat-treated and manipulated to create the undulate blade, while the rest were left untreated as they as flat blades, see Figure 3.1. To create the undulate shape, the models were held in place in the middle. A small section of the side was heated before force was exerted in opposite directions so that it was elongated. This was done a number of times throughout the length of the blade, elongating the sides and creating the undulate shape.

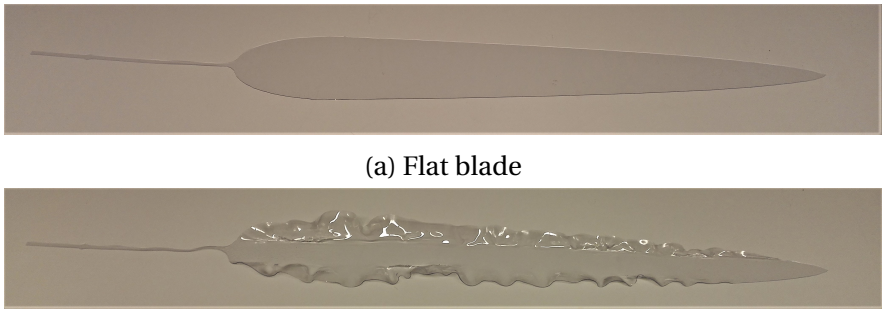

(a) Flat blade

(b) Undulate blade

Figure 3.1: Small models used in the experiment.

3.2 Laboratory Setup

The experiments were conducted in the Marine Cybernetics laboratory at the Department of Marine Technology, NTNU. The Marine Cybernetics laboratory consists of a wave basin with advanced instrumentation package and a towing carriage. The basin is 40 [m] x 6.45 [m] x 1.5 [m] (LxBxD). Video recordings were made during the drag experiment under water to see the motion of the models. Grids with yellow background and black lines with a length of 200 [mm] x 100 [mm] were used to help better separate the models from the background and to ease any measurements.

Drag force, speed and acceleration were recorded during the towing experiment. Single

point load cells, PW2C, were used to measure the drag force. Current meter data available at *yr.no* was used to find appropriate carriage velocities for testing. Vettori (2016) used current velocity recorded in Loch Fyne, a seawater loch located in South-West Scotland, where the *L. saccharina* samples were harvested. The mean current velocity was found to be 11.1 [cm/s] with the lowest and highest recorded values being 1.4 [cm/s] and 57.8 [cm/s] respectively. Similar current velocities are found in the areas of interest, with an mean current velocity around 10 [cm/s]. The carriage was set to run at the velocities of 10, 20, 30, 50 and 70 [cm/s] for the large model. For the small model 100 [cm/s] runs were also performed. However, the average recorded velocities was somewhat higher for all runs, 10.2, 20.5, 30.7, 51.2, 71.7 and 102.4 [cm/s].

Two setups were made. One simple setup and cylinder setup, see Figure 3.2. The drag force was measured for 30 [s] before each run was started. The carriage was then rapidly accelerated to the appropriate speed. After reaching the end of the basin, the carriage was put in reverse and moved back to its original position and left for 2 [min] before a new run was executed in the same manner as described above.

(a) Simple setup

(b) Cylinder setup

Figure 3.2: The carriage and setups in the Marine Cybernetics laboratory.

3.2.1 Simple Setup

Figure 3.3 shows the 3D drawing of the simple setup made by Trond Innset.

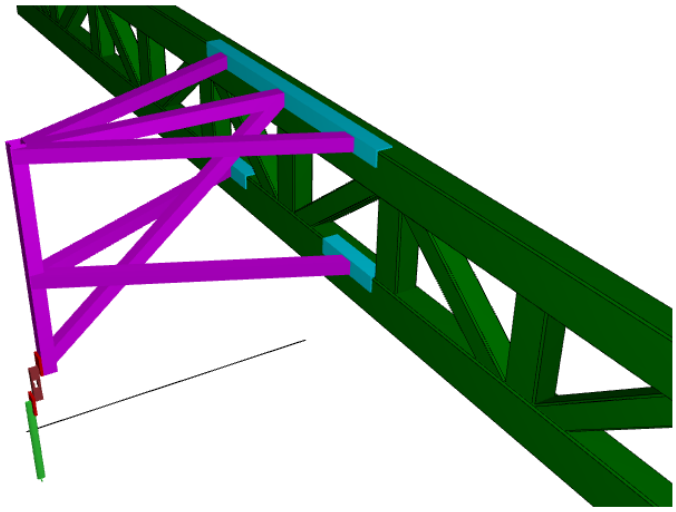

Figure 3.3: Simple setup attached to the front part of the carriage (green). Load cell (burgundy) is attached between the main part of the setup (purple) and the profiled rod (light green).

At the bottom of the profiled rod a screw eye was attached, see Figure 3.4. The distance between the water surface and the middle of the screw eye was 236 [mm]. When the setup was dragged trough the water without any models attached, a plug was inserted into the hole. Single models were attached to the simple setup by tying the model stipe to a screw eye and inserting the plug in the eye of the screw.

Figure 3.4: Close-up of profiled aluminum rod with the screw eye inserted at the bottom.

Figure 3.5 shows patch scale of the simple setup, from here on out referred to as clusters. The stipes of the 9 models were tied to a screw eye similarly to a single model, but did not have a plug inserted into the screw hole.

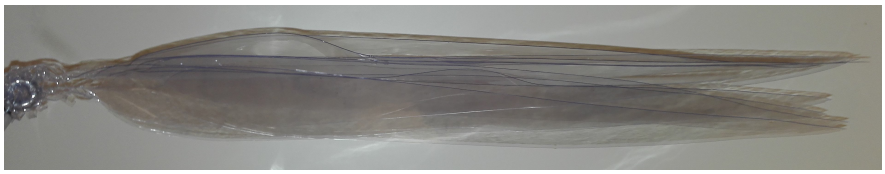

(a) Patch of flat blades

(b) Patch of undulate blades

Figure 3.5: Simple patches of 9 small blades referred to as clusters.

3.2.2 Cylinder Setup

Figure 3.6 shows the 3D drawing of the cylinder setup made by Trond Innset. The cylinder setup had an upper arm of 2106 [mm] from the hinge to the load cell, and a lower arm of 346 [mm] from hinge down to the middle of the cylinder under water. The cylinder was 500 [mm] long with a diameter of 4 [mm].

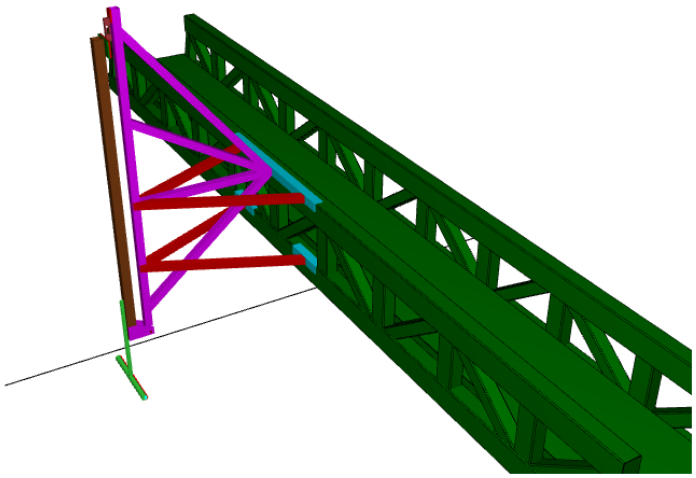

Figure 3.6: Cylinder setup attached to the front part of the carriage (green). Load cell (burgundy) at the top of the contraption is attached between the main part of the set-up (purple) and one end of the long arm (brown). The other end of the long arm is attached to a hinge (purple) and the profiled rod with the cylinder on the other end (light green). Curved plates (deep red) had models attached to them before being mounted on the cylinder.

For the cylinder setup, the model stipes were tied to rings attached to curved plates with

the same curvature as the cylinder was made, see Figure 3.7. The distance between the water surface and the center of the cylinder was 250 [mm]. There was two rows with 14 and 15 rings on the upper and lower row respectively. The angle between the rows were approximately 80° and the midpoint between the rows was aligned with the incoming fluid flow. The setup alone without models had a curved plate with rings attached to it when dragged through the water for drag force measurements. The sides of the cylinder was closed off to allow dye inserted into the cylinder to only exit at holes made on its surface.

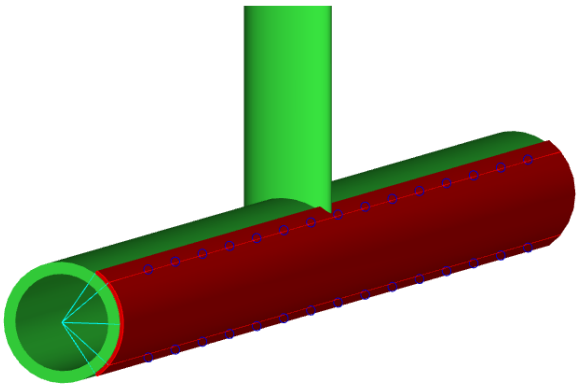

Figure 3.7: Close-up of profiled aluminium rod and cylinder with curved plate (deep red) and rings (blue) for attaching the model stipes.

3.3 Post-Processing of Data

3.3.1 Filtering of Noise and Vibrations

Highly sensitive load cells were used, with a sampling frequency of 50 [Hz]. High sensitivity can be a drawback when measurements are performed in an environment with significant vibrations, such as the Marine Cybernetics laboratory. The main contributor to these vibrations seems to be the start-stop motion of the carriage itself during the runs, as was discovered during the preliminary tests. The stop-start motion is due to friction between the tracks and wheels, and leads to deceleration and acceleration of the carriage rather than a constant velocity. Figure 3.8 shows one example of how much the speed and acceleration fluctuated throughout a run.

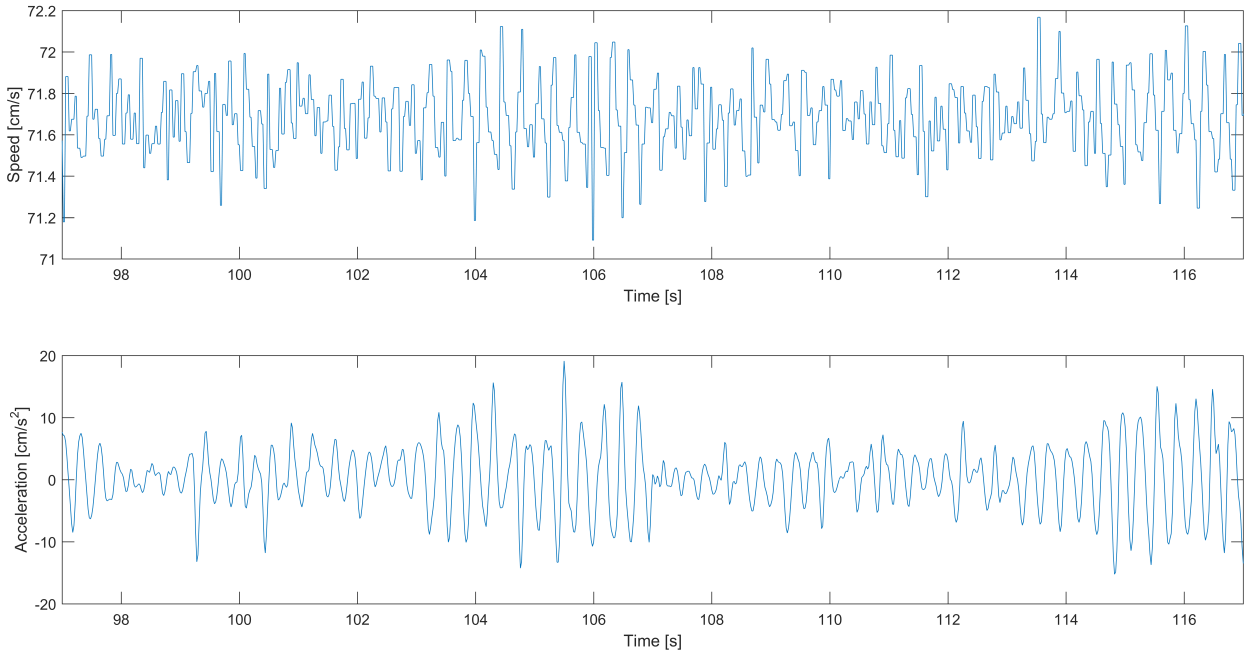

Figure 3.8: Fluctuation of speed and acceleration during a run set to 70 [cm/s].

The noise and vibrations introduced by the facility was mitigated by the use of a low-pass filter. The low-pass filter allowed for high frequency disturbances to be removed without influencing mean values and removing low frequency changes. Butterworth filter available as a MATLAB function was used. The order of the filter was set to 2 and the cut-off frequency to 0.5 [Hz] divided the Nyquist frequency. The cut-off frequency was chosen so that it did not influence the lower frequencies of the power spectral density when only looking at the steady part of the run, see Figure 3.9. This was to make sure that the mean values were not distorted during the filtering process. Due to their small sampling size, the highest speeds, i.e. 71.7 [cm/s] and 102.4 [cm/s], were used to evaluate the cut-off frequency. The whole run, including when the carriage was not moving and transient parts, was then filtered and used for further processing, see Figure 3.10.

Decay tests were performed and showed that the setups attached to the carriage had a natural frequency in the 1-4 [Hz] range. This is above the cut-off frequency. From Figures 3.9 and 3.10 it can be seen from the power spectral densities that this is a region with a lot of energy.

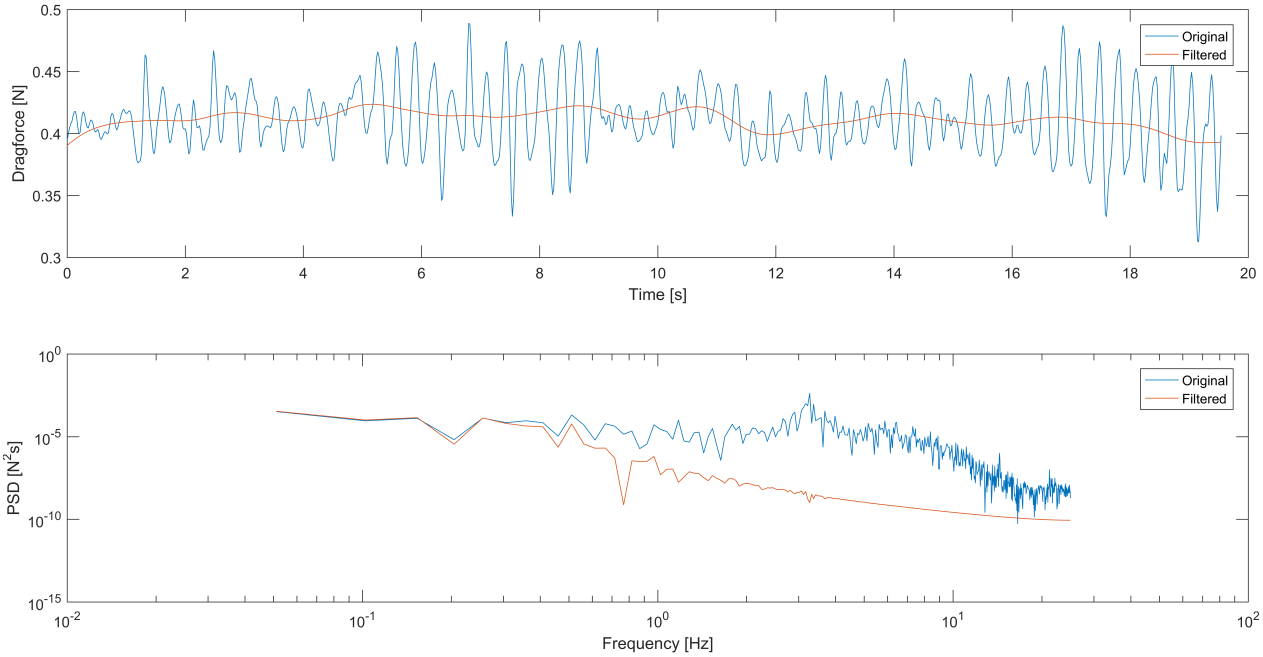

Figure 3.9: Visualization of the steady part of the run and power spectral density for evaluation of the order of the filter and cut-off frequency on the simple setup at 71.7 [cm/s].

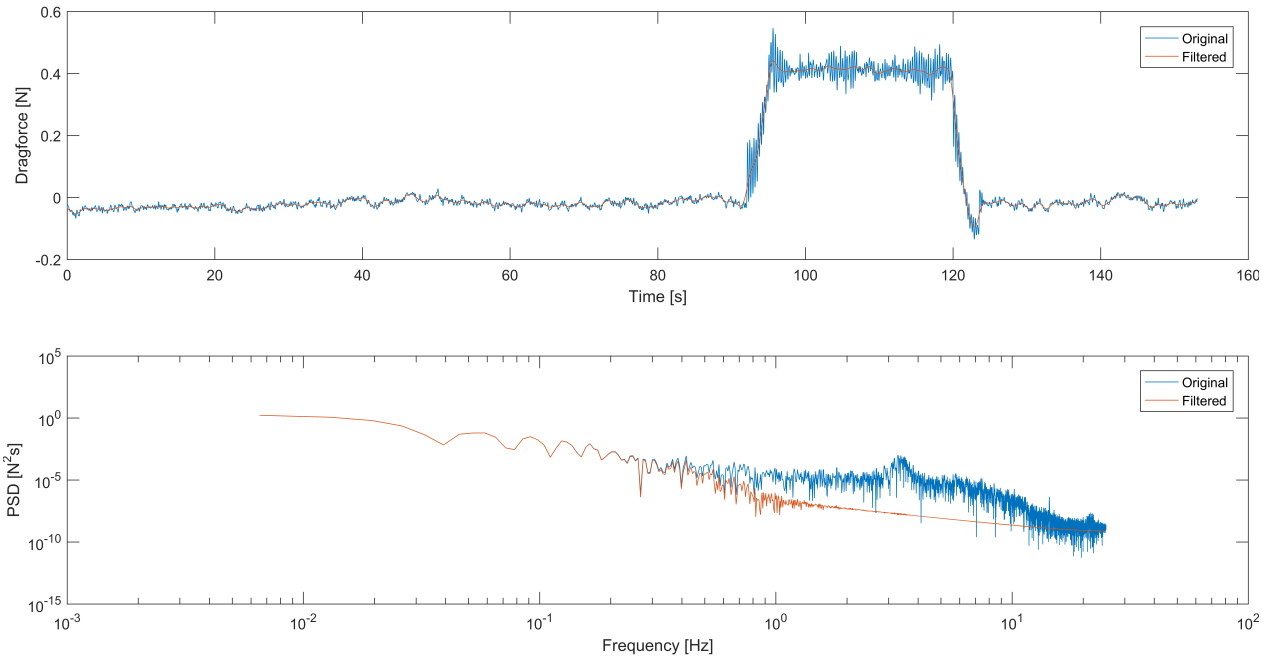

Figure 3.10: Final filtering of the drag force measured on the simple setup at 71.7 [cm/s].

3.3.2 Drag Force, Drag Coefficient and Vogel Exponent

After the drag force data had been filtered, the following steps were performed with MATLAB as the tool. The drag force measured before each run was used to find the mean difference from zero drag, and subtracted from the whole time series. This was done for each time series. The mean drag force recorded at each point of the run of the setups alone was then removed from the drag force recorded for the runs with models attached. To find the mean drag force, transient parts due to acceleration and deceleration of the carriage were removed, before finding the total mean and standard deviation of the three runs for each speed. It was assumed that no force was lost trough deformation of the setup or due to friction.

For both the flat and undulate model the original projected area, as described by the CAD model used to cut their outline, was used for finding wetted surface area. Thickness was neglected and wetted surface area was said to be twice this projected area. Due to the process of making the undulation, the undulate blade will have a larger wetted surface area then the one found with this approach. For the patches, the wetted surface area was said to be the total wetted surface area of all the blades in the patch combined.

The Vogel exponent was found using the method described in Section 2.4.2. The logarithm of the drag force divided by the square of the speed was plotted against the logarithm of the speed. Linear regression was then used to find the slope, i.e. the Vogel exponent.

3.3.3 Underwater Video Footage

Distortion was mitigated through a script in MATLAB written by Aurélien Liné. Afterwards the files were imported into ImageJ, where brightness and contrast were tweaked to distinguish the models from the background. For measurements of the mean angles the files were converted to grey scale before tweaking contrast. Angles were measured by looking through the videos and finding a mean value when the model or cluster had a steady behavior.

Chapter 4

Results and Discussion

This section contains the results and discussion of the experiments conducted during this master thesis. To help differentiate the different scales and models, the same color coding and markers have been used throughout, see Figure 4.1. Colors show the different blade type as well as scale. Red for undulate patches, blue for flat patches, yellow for undulate single blades and green for flat single blades. Markers show the size of the models, with triangles signifying small models and circles signifying large models. Patch scale for the simple setup is referred to as a cluster, due to its formation.

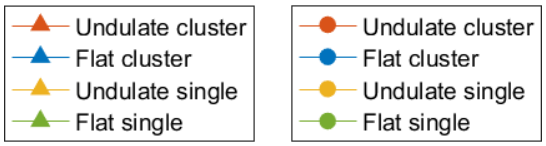

(a) Small model (b) Large model

Figure 4.1: Example of color coding and markers used for the different models and configurations.

Due to the stop-start motion of the carriage during the runs, the velocity was not constant and acceleration was different from zero. This lead an added force component in the form of added mass. However, due to the seemingly sinusoidal nature of the vibrations of the carriage, and that the mean acceleration was zero, the added mass should not influence the mean drag values (White, 2011). Hence it is not considered further in this master thesis.

4.1 Drag Force

The development of the mean drag with increasing speed for the small and large blade model can be seen in Figure 4.2. Note that the standard deviation is the variation of the filtered values, not the measured values. The reason for this being that the uncertainty in the measured values was not of primary interest. Instead, the standard deviations were used to look at how the blades moved differently for different values. As expected, the drag force for the undulate blade model in both blade and patch, i.e. single model and cluster respectively, are larger than the flat blade model when dragged at the same speed. This is the case for all velocities, except for the lowest, 10.2 [cm/s], where the flat and undulate model experience similar drag force in both blade and patch scale. For both small and large models, a cluster of flat blade experience a similar drag force as a single undulate blade, with the exception of the two lowest velocities. One interesting observation is that the mean drag force decreases for both flat model clusters from 10.2 [cm/s] to 20.5 [cm/s]. This could be due to large decrease in the angle between the cluster and the fluid flow, causing a large reduction of pressure drag due to separation, see Section 4.2.

It seems like the drag force for the clusters do not approach zero with decreasing speed, as it seems to do for the single models. The large difference between the drag force measured at 10.2 [cm/s] between the single blades and clusters could be due to the setup having to be somewhat altered for the attachment of the clusters compared to a single blade and the setup alone, as mentioned in Section 3.2.1. It is possible that the lack of a plug, and the streamlining it entailed, caused an increase in drag force. Another possibility is that the increase in frontal area at the screw, caused by tying the stipes to the screw eye, led to the increased drag. Either way, this would lead to a systematic error, with drag force measured to be higher than its true value Steen (2014). This systematic error would be most prominent at the lower velocities, due to their overall lower experienced drag. By doing runs of the setup alone with the tied part of the stipes without the blades themselves and without the plug, the mean drag force would likely have been smaller. This because the aforementioned systematic error should have been reduced.

The standard deviation of the undulate clusters had a visible increase with increasing speed. As an example, the large model standard devation at 71.7 [cm/s] was 33 times larger than the standard deviation at 10.2 [cm/s]. For comparison, the mean drag force at 71.7 [cm/s] is 14

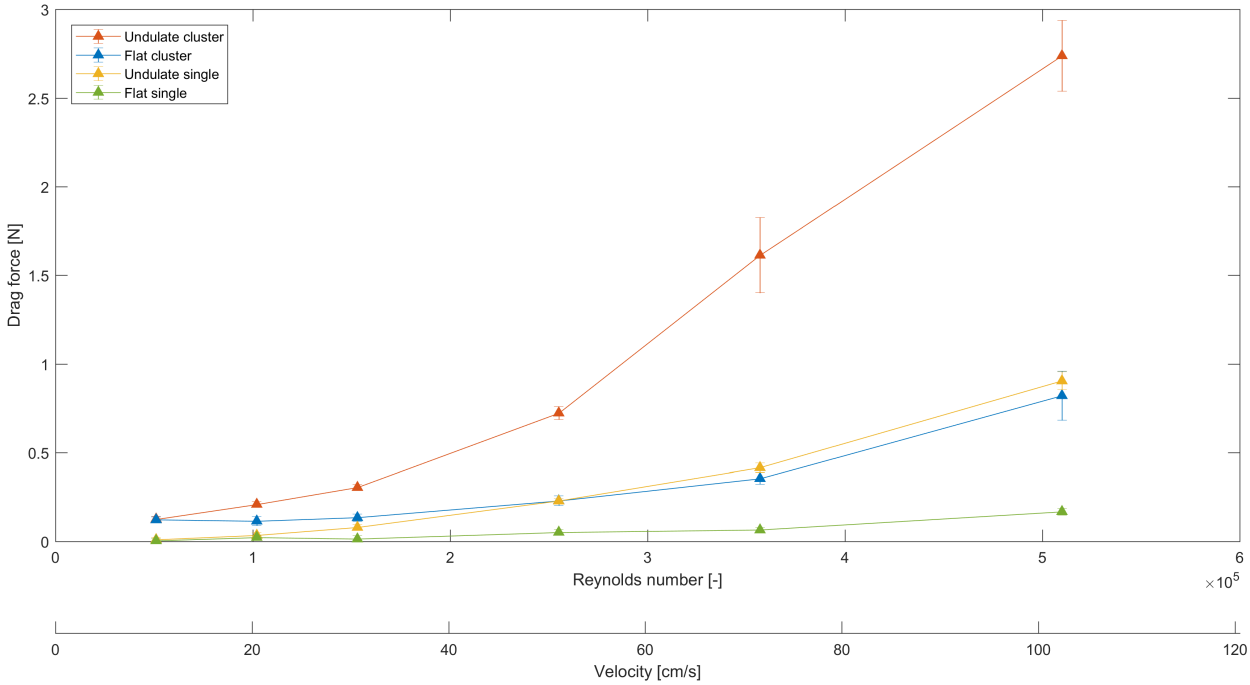

(a) Small model

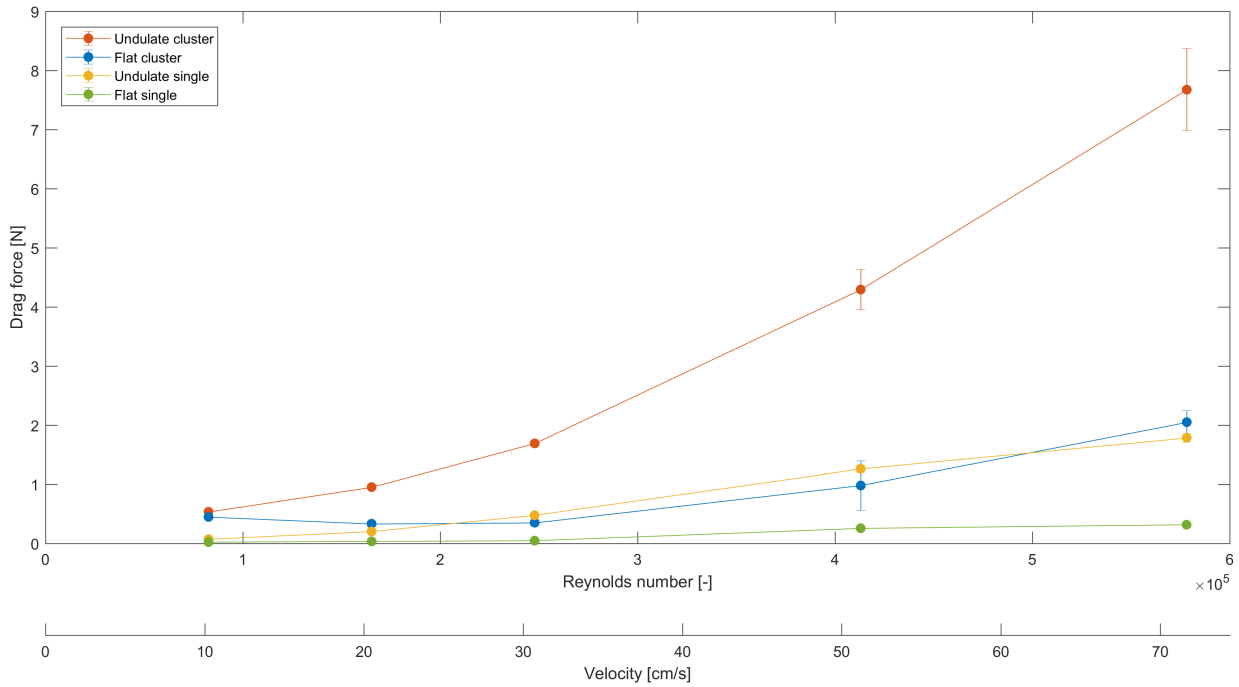

(b) Large model

Figure 4.2: The mean drag force and standard deviation at different speeds for single models and clusters of undulate and flat blades. The means and standard deviations were found from the filtered values.

times larger than the mean drag force at 10.2 [cm/s]. Figure 4.3 shows the development of the drag force at 51.2 [cm/s] and 71.7 [cm/s] for the small model clusters during each of the three runs. It can be seen that the runs of the flat cluster are repeatable, exhibiting similar behavior each time. In contrast, looking at Figure 4.3b, undulate cluster behavior at 71.7 [cm/s] does not repeat. There is a larger variation between individual runs, causing the large standard deviation of the mean value. At 102.4 [cm/s] similar unrepeatable behavior was seen for the flat blade cluster, again reflected by the increase in standard deviation. The larger standard deviation at 51.2 [cm/s] however, seems to be due to reconfiguration of the cluster rather than lack of repeatability, as there is a visible reduction in drag force throughout the run, see Figure 4.3a.

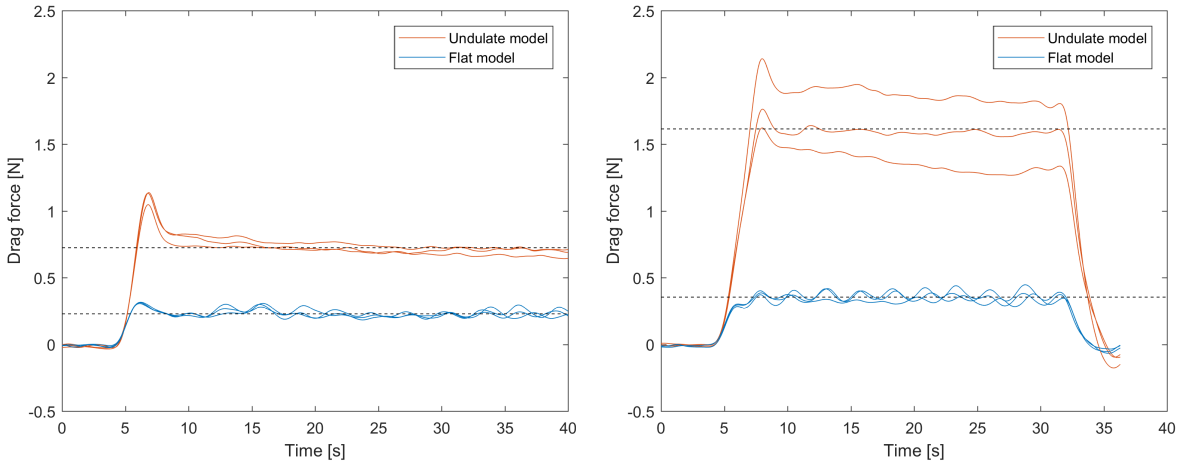

(a) $U = 51.2$ [cm/s], $Re = 2.55 \cdot 10^5$ [-] (b) $U = 71.7$ [cm/s], $Re = 3.75 \cdot 10^5$ [-]

Figure 4.3: Filtered drag-force development for small-model clusters. The dashed lines mark the mean drag force for the non-transient part of the runs.

Figure 4.4 shows the development of drag force for the large clusters at similar Reynolds numbers, although somewhat lower and higher than the Reynolds numbers of the small clusters in the previous figure. For the lower speeds the flat cluster has visible oscillation, though not as regular and prominent as for the small model, see Figure 4.4a. At higher speeds, a similar lack of repeatability, as seen for the small undulate cluster, was seen for the large undulate clusters, see Figure 4.4b. Again the reason for the increase in standard deviation at higher velocities seems to be due to this lack of repeatability. From video footage it could be seen that the odd run of the flat model cluster seen in Figure 4.4b likely was due to the models previously sticking together slipped due to the high velocity, before sticking together again causing the transient increase in

drag force.

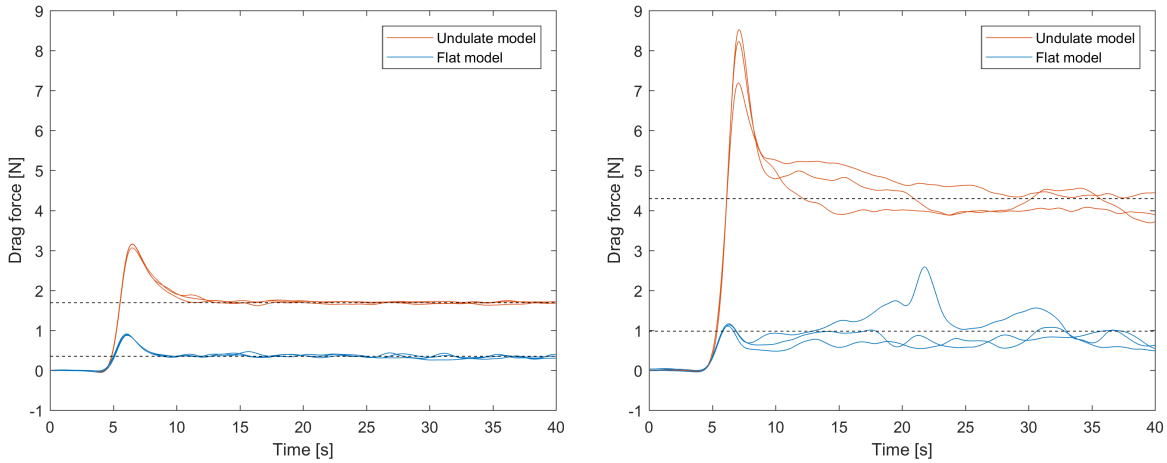

(a) $U = 30.7$ [cm/s], $Re = 2.48 \cdot 10^5$ [-] (b) $U = 51.2$ [cm/s], $Re = 4.13 \cdot 10^5$ [-]

Figure 4.4: Filtered drag-force development for large-model clusters. The dashed lines mark the mean drag force for the non-transient part of the runs.

When looking at the behavior of the drag force for flat and undulate single blades, it was difficult to say if there was an oscillation of the drag as was seen for the flat clusters. The variation of the drag force was not as distinct as for the flat clusters and could be due to noise. The drag force measured at 10.2 [cm/s], 20.5 [cm/s] and 30.7[cm/s] for the small flat blade was 0.0037 ± 0.0112 [N], 0.0227 ± 0.0105 [N] and 0.0136 ± 0.0179 [N] respectively. These large standard deviations compared to mean values makes any definite observation about the development and trends of the drag force at these small velocities inconclusive for the blade in question.

When considering the models for use in assessing the hydrodynamic properties of seaweed farms, their hydrodynamic properties at both blade and patch scale will be of importance. Looking back at the mean drag development in Figure 4.2 there is little difference in drag force for both the blades and clusters at 10.2 [cm/s], which is close to the mean expected current in areas of interest and the mean current found in Loch Fyne where Vettori (2016) harvested in his *L. saccharina* samples. At these velocities there seems to be little difference between the models, and if only drag force is of interest then the flat blades might be good substitutes for the more time-consuming process of preparing the undulate models. Even so, it should be noted that the drag experienced by the large undulate cluster is 20 % higher than the large flat cluster. Also, when considering that the highest speed recorded in Loch Lyne was 57.8 [cm/s], higher speeds

should be considered when assessing if flat blades can be used as a substitute. At 30.7 [cm/s] and 51.2 [cm/s] the drag for the large undulate cluster is 4-5 times greater than that of the large flat cluster.

4.2 Mean Angle and Visual Behavior

Figure 4.5 and 4.6 show stills from the video footage taken during some of the runs for the small and large model respectively. Superimposed on the stills are the mean angles of the single blade or cluster during the run, showing how the mean angle develops with velocity and Reynolds number, and how they compare for the different models. Due to limited battery time of the underwater camera and some issues with the carriage not going at the appropriate speeds, some data points are missing. At the beginning of the run the angle between the fluid flow and the model decreased quickly. Often the model moved above the line drawn parallel to the flow before going back down to a steady angle.

When looking at the same speed at blade scale, the large model has a smaller, but similar, mean angle to the flow compared the small model. However, looking at similar Reynolds numbers, the mean angle of the large model at blade scale seems to be larger. Unfortunately, there are not many data points to compare, so it is difficult to come with any conclusive remarks. In contrast, is seen that at patch scale, where the large cluster has a larger mean angle than the small cluster for both speed and Reynolds number. However, it should be noted that the mean angles are close to each other in value, and differences could be due to mistakes in measurements.

For all models, both in single and cluster, the mean angle is reduced with speed. The only exception for this being the single large flat model run at 51.2 [cm/s]. During this run the blade fell to the side, making its thickness meet the flow, rather than its width. The mean angle of this run is therefore not representative, but shows a phenomenon that can occur for the flat blade. At blade scale, the undulate model has a larger mean angle than the flat model. Contrary to this, at patch scale, the undulate cluster has a smaller mean angle than the flat cluster. This is true for all speeds with the exception of 20.5 [cm/s] for the small model.

At lower velocities, there was visible bending of the models. This bending becames smaller as

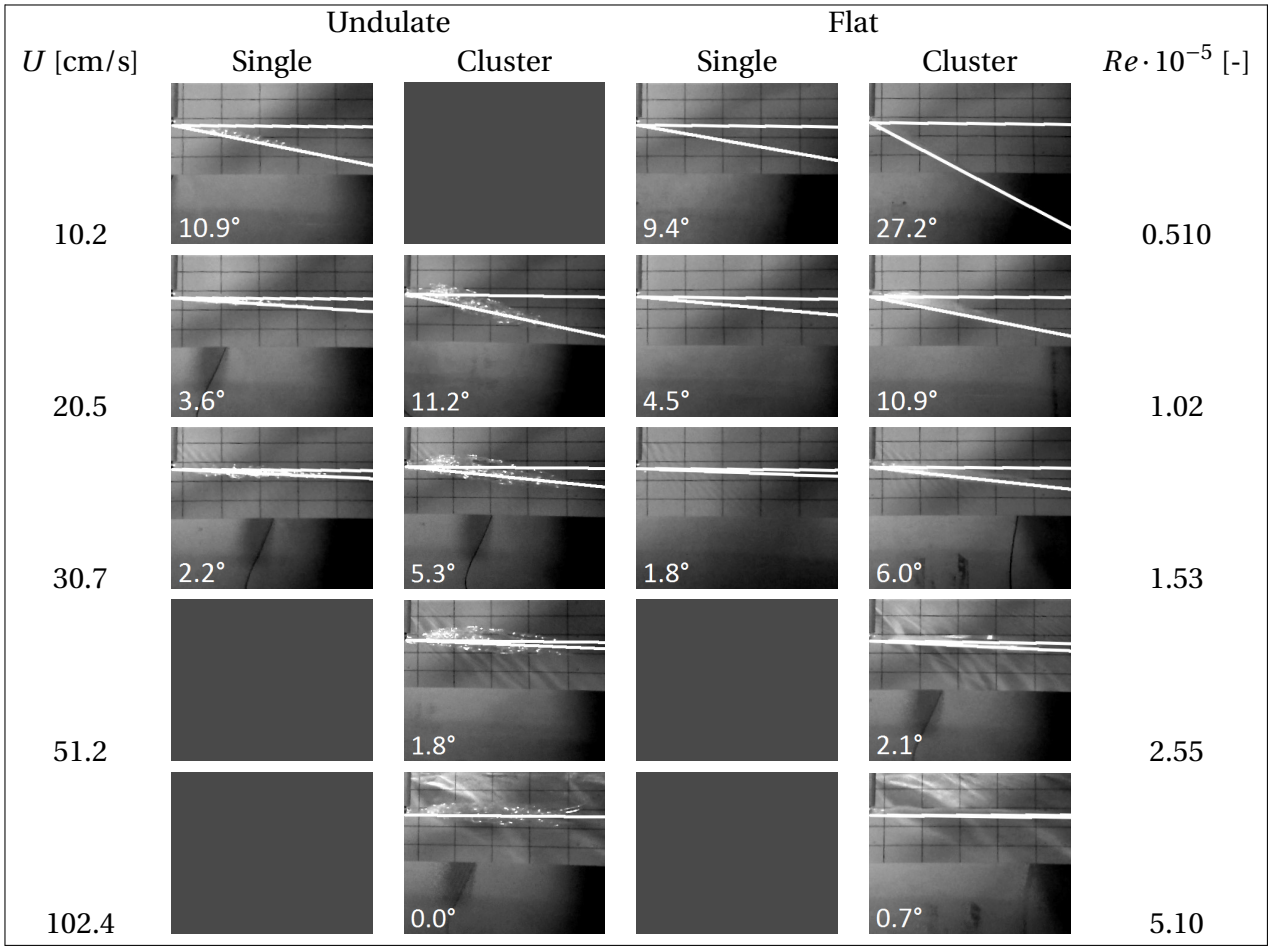

Figure 4.5: Stills with the mean angle of the blade or cluster from the video footage taken during the different runs of the small plant.

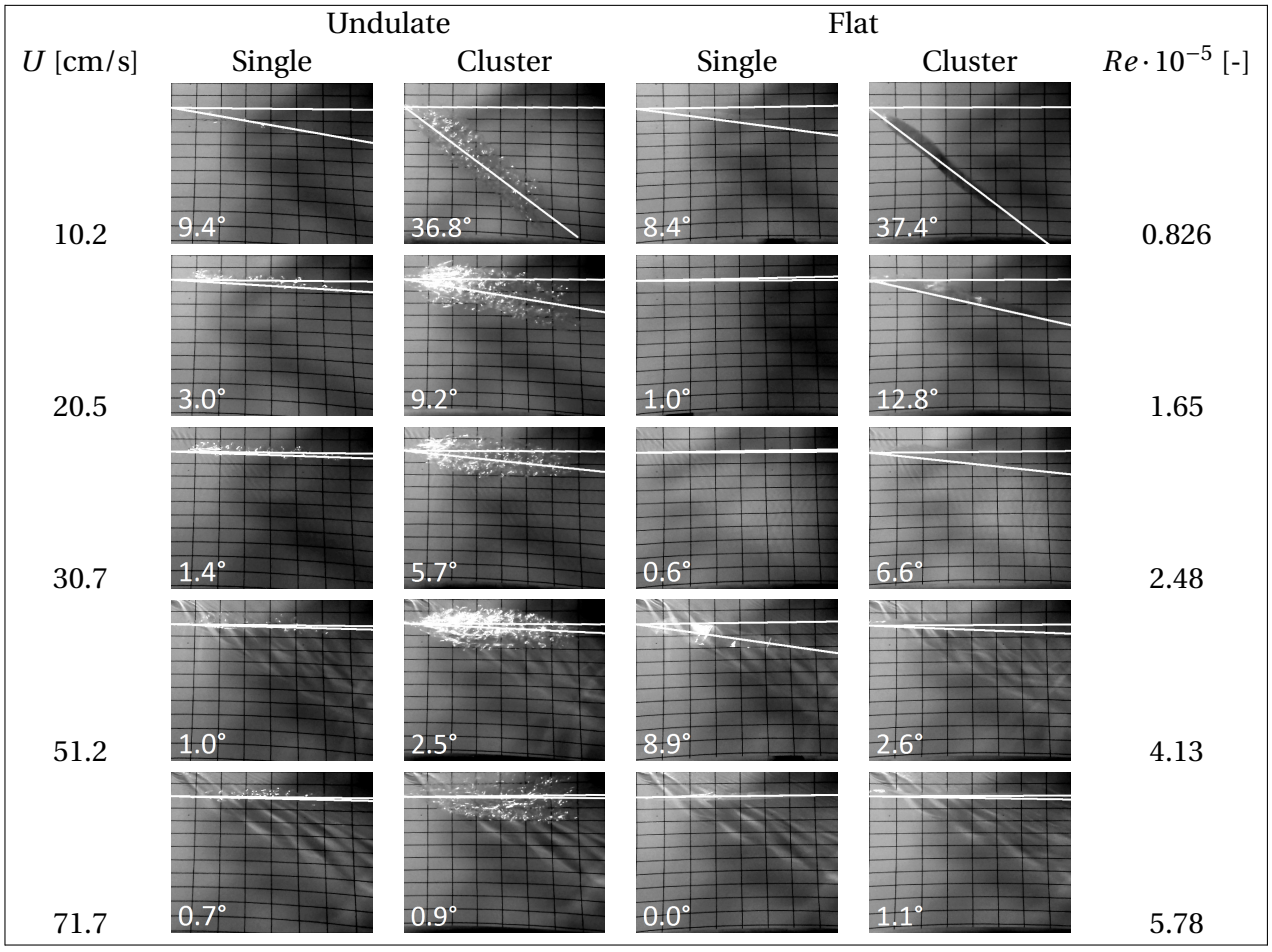

Figure 4.6: Stills with the mean angle of the blade or cluster from the video footage taken during the different runs of the large plant.

the angle decreased and there was no visible bending at the highest velocities. As mentioned by Nikora (2010) plants can be divided into two extremes; 'tensile' and 'bending' plants. At different velocities, the models behaved visible different, and their behavior can be categorized as mainly 'bending' plant at lower velocities, and as 'tensile' plant at higher. While the drag experienced by the 'bending' plant will mainly be associated with pressure drag, the drag of 'tensile' plant will be due to friction drag. Additionally, when the models become close to parallel to the flow, they might act similarly to a flag, and experience increased drag due to fluttering Hoerner (1965).

For the small undulate model there was no visible motion for the speeds 10.2 [cm/s] to 30.7 [cm/s]. Higher speed videos are not available, with the reason for this being previously mentioned. For the large undulate model, there was also no visible motion for the two lowest speeds. At 30.7 [cm/s] the model had some visible motion, both rotation and what seemed to be fluttering. At 51.2 [cm/s] the model had a lot of rotation, but seemed to have somewhat collapsed on itself. Finally, at the highest recorded speed for the large undulate blade, 71.7 [cm/s], there was much less motion and it still looked somewhat collapsed.

The flat single models had a lot of motion in the form of rotation, and were in general very unstable. Sometimes the models fell to the side so the thickness met the fluid flow. There was then much less motion. In this position the blade would act as a 'tensile' rather than 'bending' plant even at lower speeds. For the large model at 51.2 [cm/s] there was visible waves propagating though the blade. At 71.7 [cm/s] the large flat blade collapses on itself.

For the undulate clusters there was little visible change during the runs at lower speeds. With increasing speed there was more visible movement. Even so, for the small model cluster, the motion did not move past the tips of the blades. For the large models however, there was visible change in the projected area of the cluster during the runs. At 51.2 [cm/s] the cluster did not reach a steady state but continuously rotated and changed its density during the run, see Figure 4.7. This is likely the reason for the large difference between the runs at this speed, see Figure 4.4b. At 71.7 [cm/s] the large cluster seemed to spread out more and remained in a somewhat stable position.

From the video footage taken under water it can be seen that the flat cluster, both small and large models, to a large extent stick together to form one entity. At lower speeds a pendulum-like motion was observed. The blades, while sticking together, moved side-to-side while being

dragged through the water. This is likely the reason for the observed oscillation of the drag force, see Figures 4.3 and 4.4. At higher speeds the cluster was almost parallel to the flow, making it difficult to detect the presence of any pendulum motion. However, fluttering motion was observed. Even though there were many similarities between the behavior of small and large flat clusters, some differences were observed.

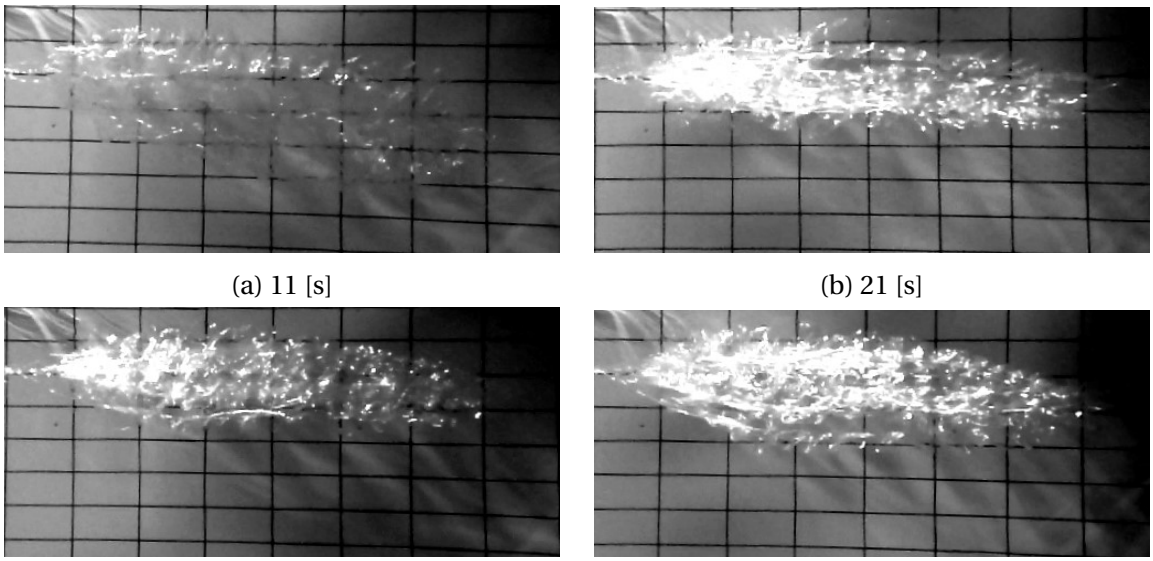

(a) 11 [s] (b) 21 [s]

(c) 26 [s] (d) 37 [s]

Figure 4.7: Visible change of the undulate cluster during the run at 51.2 [cm/s].

The small flat models clustered together, however, when dragged through the water individual blades could clearly be seen. At 10.2 [cm/s] the individual blades spread apart at the ends. The point of visible separation between the blades moved upwards with increasing speed. This continued up to 51.2 [cm/s]. At 71.7 [cm/s] however the individual blades could still be seen, but the patch as a whole moved more as a single entity, or blade.

Similarly, for the large flat model cluster at 10.2 [cm/s] the blades were together except for at the tip. However, at 20.5 and 30.7 [cm/s] the blades seemed to stick together, with only a few freely moving blades at the top towards the water surface. The patch was also divided into two parts that joined each other towards the blade tips. This might not have been true for later runs for which the drag force was recorded. At 51.2 [cm/s] the patch moved more or less as one entity, and individual blades could not be seen, similar to what was seen at 71.7 [cm/s] for the small blade. The large model at 71.7 [cm/s] moved as one entity, but sometimes it fell apart before

clustering again.

From the previous paragraphs it can be gathered that the flat and undulate blade have distinctively different behavior. While the flat blades to a large extent collapse and move as one entity, the undulate blades remain separated in the flow. Additionally, the flat blade is much more unstable in the flow, while the undulate is more stable with much less movement. This is likely due to how the boundary layer develops across the blades. For the flat blade, a large vortex is allowed to be developed and when shedded at its tip, causing a large change in momentum and therefore large motion (Hoerner, 1965). It is however likely that these large vortices cannot develop on the undulate due to its shape. Instead smaller vortices will be formed in its valleys(Hurd et al., 1997), and there will be no large momentum changes and motions such as those seen for the flat blade. Unfortunatly, the flow over single blades was not visualized and these are only assumptions taken from what has been seen in previous studies and known fluid-dynamic phenomenons.

4.3 Drag Coefficient

The drag coefficients in Figure 4.8 were found using wetted surface as the characteristic area, making comparison of the patch drag coefficients with the single model drag coefficients easier. However, the wetted surface of the undulate blade is underestimated. As a consequence, its drag coefficients are overestimated. Figure 4.8a and 4.8b show how the drag coefficients develops with increasing velocity for the small and large model respectively. For the single blades at lower speeds, especially for the small models, there is a large standard devation, due to the mean drag being small compared to its standard devation and the speed at which it was measured.

There is a similar trend for the small and large model, with the single undulate blade having the largest drag coefficient, about twice that of the undulate cluster. The flat cluster has the smallest drag, but larger compared to its single plant than the undulate cluster. With the use of wetted area as the characteristic area of the drag coefficient, it was expected that it would be smaller for the cluster than the single blade. This is due to self-shading within the cluster, causing the mean fluid speed experienced by all the blades to be smaller than that of a single blade. When comparing the drag coefficient of the singles to the clusters from when they have become

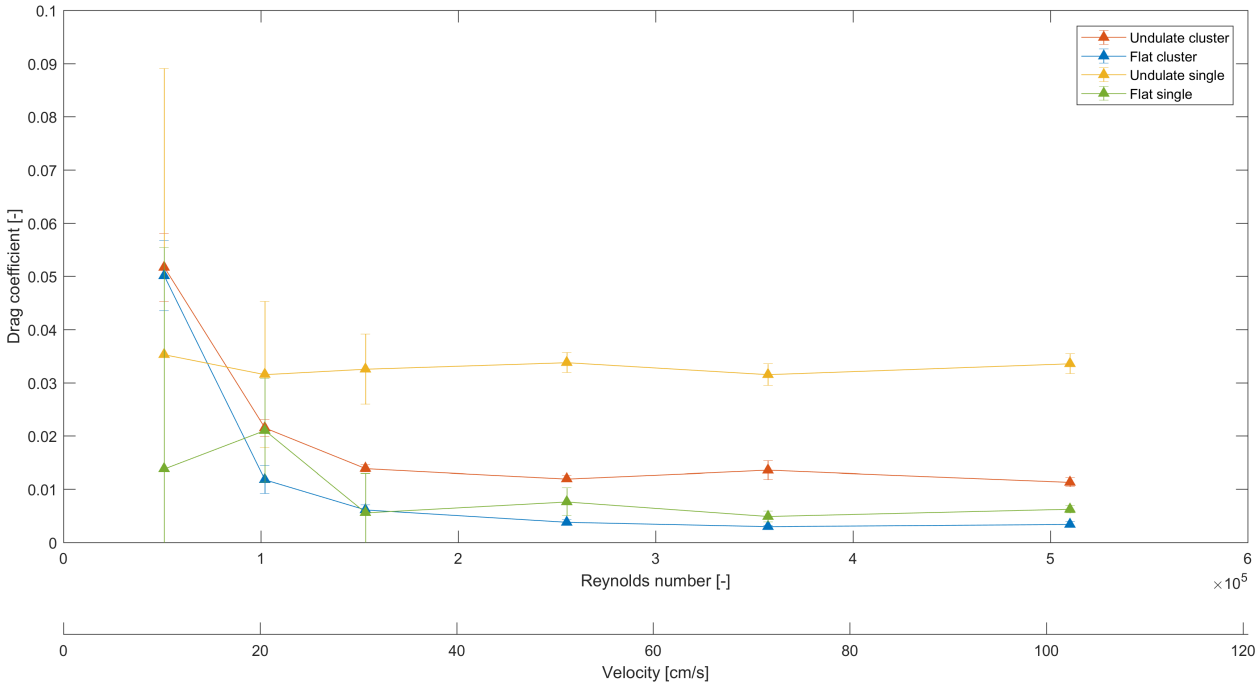

(a) Small models

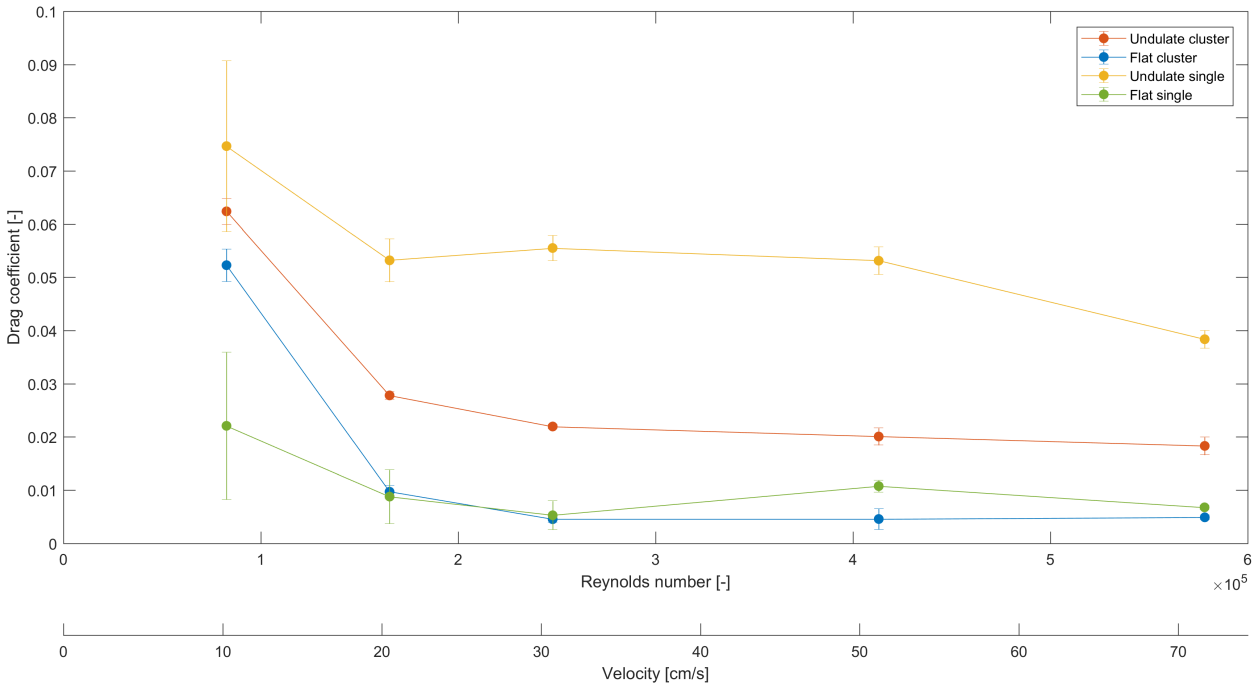

(b) Large models

Figure 4.8: The drag coefficient with wetted surface as the characteristic area.

relatively stable in value, the undulate single blades have a drag coefficient approximately 2.5 times larger than its cluster, and the flat blades 1.6 times larger. From this it seems that the undulate blades experience more self-shading. From looking at the video footage however, this does not seem to be the case. The undulate clusters are more spread than the flat clusters. The larger reduction in drag per blade for the undulate cluster must therefore be due to some other factor. It could be that the flat blades going together makes it behave more like one entity with higher flexural rigidity, thereby experiencing less reduction in drag via reconfiguration. Another possibility is that was be due to the observed pendulum motion.

The single blade drag coefficients does not have as large of a reduction from 10.2 [cm/s] to 20.5 [cm/s] as the clusters. From the footage, it seems like the reason for this is that the single blades mean angle is much smaller at the same speed. At these lower speeds the cluster reconfigure via bending due to the larger angle with the fluid flow. It can also in part be due to the difference in setup between the setup alone and the setup with the cluster, as mentioned previously. This added drag will have a large impact at lower speeds, due to it being a large part of the total drag. As the speed increases, it will have a smaller and smaller impact on the found drag coefficient.

The drag coefficient of both the single flat model and undulate model increase around 30.7 [cm/s] and 51.2 [cm/s] before again falling in values for the small and large model respectively. For the large flat model it was observed that at 51.2 [cm/s] it began to have more movement and also a fluttering motion of the blade itself. This was not observed for the lower velocities. At 71.7 [cm/s] there was no fluttering motion, instead it could be seen that the model collapsed on itself. This self-shading could be the explanation to the reduction in drag coefficient observed for the large model from 51.2 [cm/s] to 71.7 [cm/s]. Similar behavior was seen for the large undulate model that also collapsed onto itself at the 71.7 [cm/s].

Differences between the drag coefficient of the large and small models are likely due to the difference in aspect ratio. Morris-Thomas and Steen (2009) and Carruthers and Filippone (2005) found that the drag coefficient increased with increasing aspect ratio. The large model had a larger aspect ratio than the small model, and also a larger drag coefficient for both models and both blade and patch scale. Additionally, even though the two models have the same flexural rigidity, their areas are very different. Meaning that the large model will be exposed to larger

forces. Therefore, if looking at the flexibility compared to their size and forces experienced, the large model will act as if it was more flexible, this could account for higher drag coefficient, as flexibility can lead to much higher drag forces (Hoerner, 1965).

4.4 Vogel Exponent

From Figure 4.9 it can be seen that two Vogel exponents were found for each cluster. The reason for dividing into two regions is due to the Vogel exponent reflecting how the drag coefficient varies with fluid velocity(Vogel, 1989), and that the mechanism behind it seems to be different in the two regions. From the video footage it has been seen that the models act more like 'bending' plants at lower speeds, before acting as a 'tensile' plants at higher. For the single blades, only one Vogel exponent was found. This was in part due to the large standard deviation at the lower speeds making any definite observations difficult. The reason for the large standard deviations were that the drag force standard deviations were large compared to the mean drag forces and velocities at these points. Additionally, there were only two angles that seemed large enough to be used for the 'bending' plant Vogel exponent. The 'bending'-plant Vogel exponents, ψ_b, were found to be of much greater negative value than the 'tensile'-plant Vogel exponents, ψ_t.

As can be seen from Figures 4.9a and 4.9c, the 'bending'-plant Vogel exponents have very large negative values, with the large plant even exceeding a negative value of two. This could be due to the decrease in drag force seen for the flat clusters as they become more compact, causing self-shading, at these lower velocities. It could also be due to the possible systematic error as a result to difference in setup for the clusters discussed in previous sections. This error would become less and less prominent with increasing speed, possible leading to an overestimation of negative Vogel exponent at lower velocities.

The Vogel exponent for both flat blades and the small flat patch is similar to was has been found for a flat blade parallel to the flow, approximately -0.5 (Vogel, 1983). The small undulate blade, on the other hand, has a Vogel exponent close to zero. Little motion was seen, so it could be that the high flexural rigidity and the undulate shape made it similar to a bluff body which has a Vogel exponent of approximately zero (Vogel, 1984). On the other hand the large undulate blade has a Vogel exponent in the range of what has been seen for macroalgae (Harder

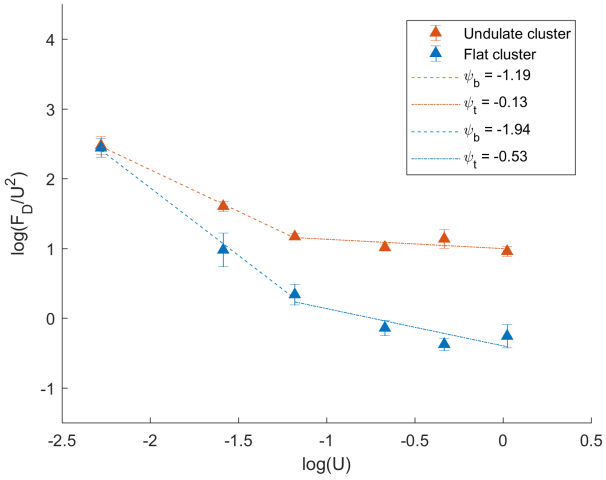

(a) Small clusters

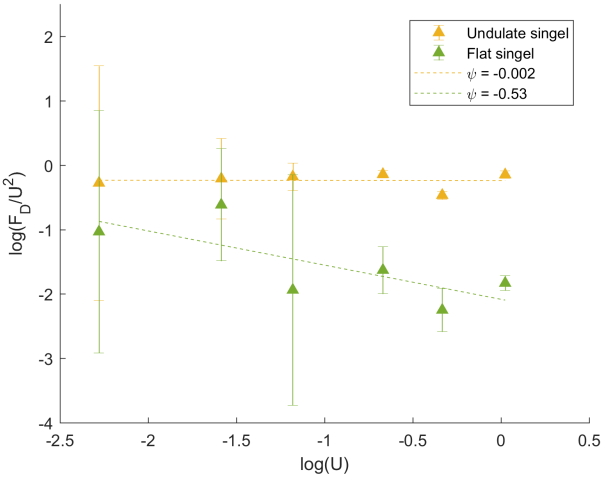

(b) Small single models

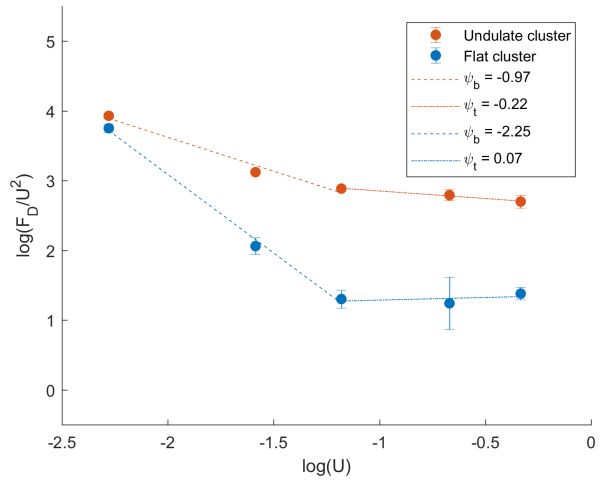

(c) Large clusters

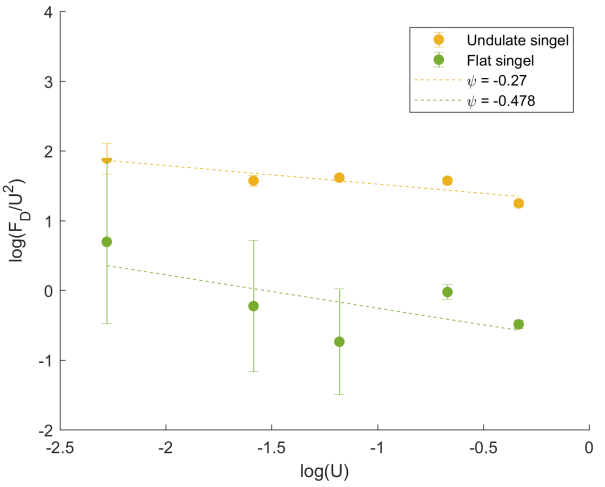

(d) Large single models

Figure 4.9: Estimated Vogel exponent for the large and small models at patch and blade scale.

et al., 2004). The same is true for the 'tensile'-plant Vogel exponent of the large undulate cluster. It therefore seems that the relative higher stiffness of the small model could possible make it unsuitable to model seaweed behavior.

At the bending stage, the flexural rigidity will be important for the drag reduction properties of the model, as high flexibility will allow for reconfiguration and thus drag reduction. On the other hand, at higher speeds, flexibility might not be beneficial. Flexible sheets have been shown to experience higher drag force compared to a similar solid sheet, due to fluttering Hoerner (1965). As fluttering motion of the cluster as a whole was observed at higher speeds, this could be the reason for the positive 'tensile'-plant Vogel exponent found for the large flat cluster.

4.5 Fluid Flow Past a Cylinder with Models Attached

The development of the mean drag force for the 29 models attached to the cylinder setu,p can be seen in Figure 4.10. Unlike the simple setup, where the incoming fluid was relatively unhindered, the incoming fluid speed experienced by the models attached to the cylinder setup was likely greatly influenced by the presence of the cylinder. The actual relative fluid velocity experienced by the models, are therefore unknown, and the Reynolds number is also unknown and therefore not shown on the graph.

Even with the patch consisting of 29 plants, the total drag was very small compared to patch scale of the simple setup, where the cluster consisted of only 9 models. Even when comparing the total drag to a single large blade, the drag was smaller. At 71.7 [cm/s] a single large model mean drag was 1.79 [N]. In comparison the total mean drag for the large undulate model patch at the same speed is 0.20 [N]. At this high speed, the patch seems to be mostly sheltered behind the cylinder. Even so, considering that a single undulate large blade experiences 0.20 [N] mean drag force at 20.2 [cm/s] it seems likely that some of the drag force has been lost in the hinge or to deformation of the arms. As with the flat cluster, the drag force of the flat patch on the cylinder is smaller for 20.5 [cm/s] than 10.2 [cm/s]. However, the drag is reduced so much that the mean is smaller than zero. It could be that the actual drag has a positive value when considering the size of the standard deviation. Another possibility is that the blades act as a splitter plate, reducing the drag on the cylinder, thereby causing negative recorded drag (Hoerner, 1965).

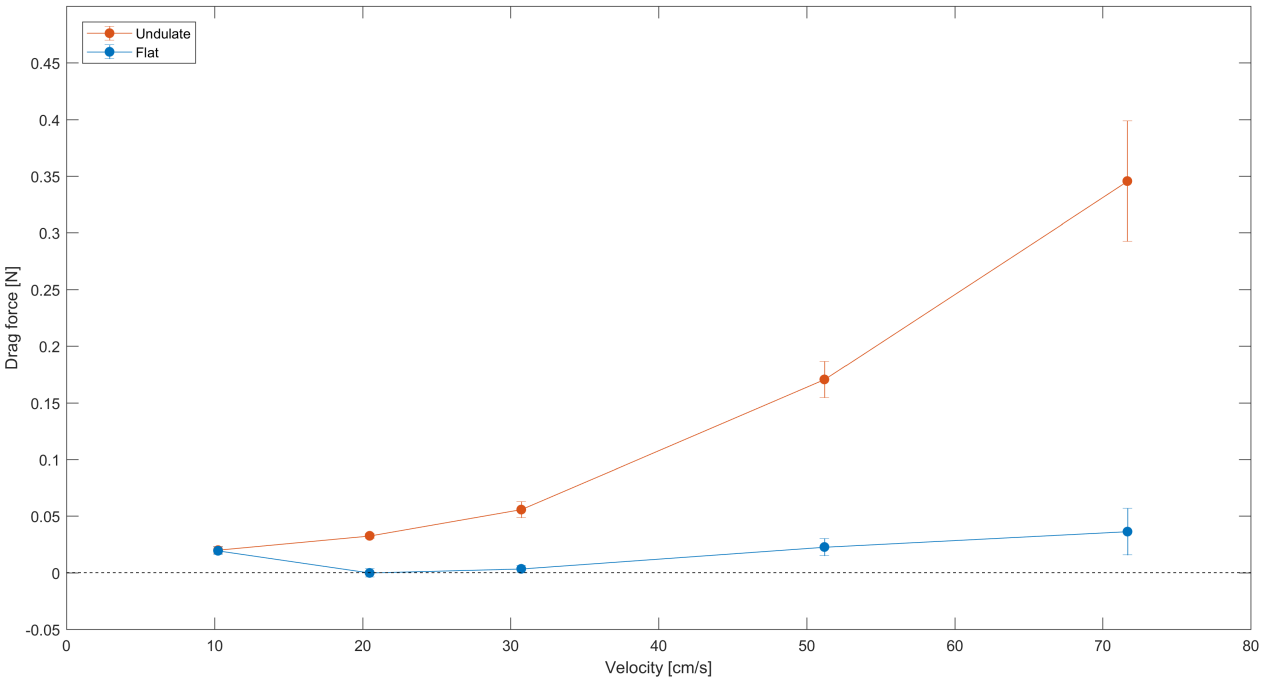

Figure 4.10: Mean drag force and standard deviation of large flat and undulate models in a patch consisting of 29 blades behind a cylinder. The means and standard deviations were found from the filtered values.

Figure 4.11 shows stills from the video footage that was recorded during release of dye to the water from inside the cylinder, while the setup was dragged at 20.5 [cm/s]. It can be seen by comparing the vortex shedding in Figure 4.11a with Figures 4.11b and 4.11c, that the presence of the models might suppress the alternating vortex shedding, as there is no Kárman vortex street when they are attached. However, it should be mentioned that the curved plate on which the models were attached was not attached during the visualization seen in Figure 4.11a. The presence of the curved plate probably influenced the flow somewhat, and most likely worked similar to a trip wire (Hoerner, 1965). A difference between the flat and undulate blade patch, is that the dye follows the whole blade length of the flat blade patch while for the undulate blade patch it does not. At this lower speed the flat patch is more shaded by the cylinder than the undulate patch. At higher speeds however, from the video footage, it seems like they are similarly exposed to the incoming fluid flow.

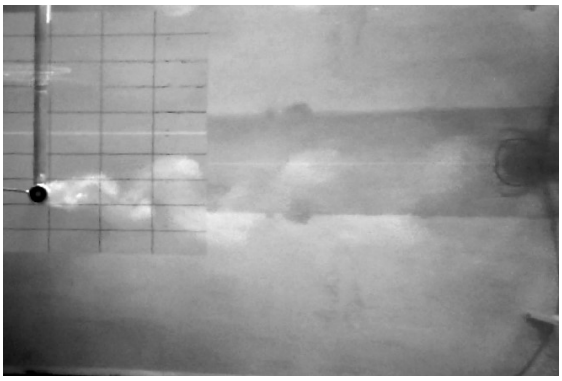

(a) Flow visualized behind the cylinder shows alternating vortex shedding.

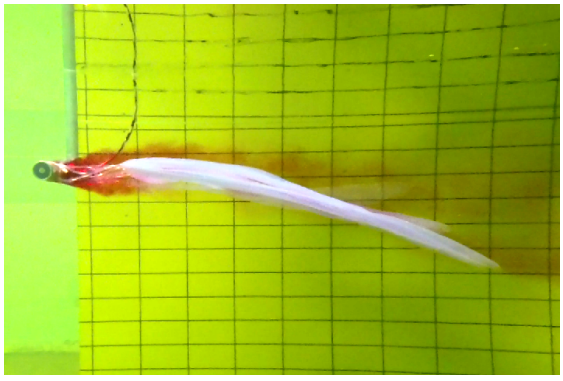

(b) The flat blades suppress the alternating vortex shedding.

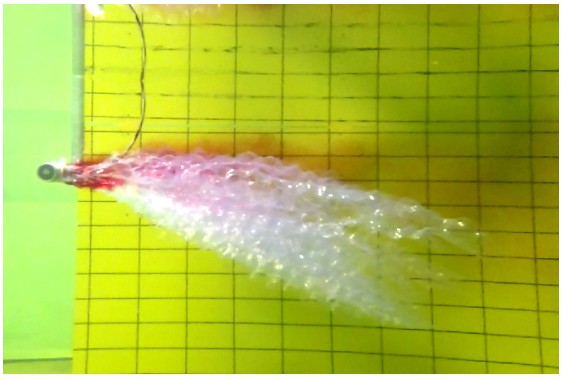

(c) The undulate blades suppress the alternating vortex shedding

Figure 4.11: Visualization of the fluid motion behind the cylinder at 20.5 [cm/s].

4.6 Evaluation of the Models as Real Kelp Surrogates

The models differ from the kelp *L. saccharina* in many aspects; both when considering material properties as well as morphological features. Even though the models used were full scale, similarity theory should be considered. While the difference in material properties makes the model not have dynamic similarity with the real kelp. Morphological differences mean that the model does not have geometrical similarity. The length and width of the blades had geometrical similarity, but the thickness had been somewhat distorted to help mitigate the difference in stiffness due to the choice of material. However, more importantly, the flexural rigidity was much higher for the models, 4.4 and 2.7 times larger for the small and large model compared to its real life counterpart respectively. This cause the models to not be dynamically similar to the real kelp, as the elastic deformations will not be the same. The difference in density is also likely to create deviations from dynamic similarity as it influences ratio between forces. Due to the lack of dynamic similiarity, there will also not be kinematic similarity. How these deviations might have influenced the results, will be discussed in the coming paragraphs.

When it comes to the material properties, PVC is denser than water, the effects of which could be seen from the video footage, with the models having an angle to the incoming fluid flow at lower speeds. *L. saccharina* on the other hand, has a close to neutral buoyancy. It is therefore likely, that the angle observed at the lower speeds would not be present had the model been made out of a material with the correct density. This is supported by the findings of Paul and Henry (2014), as they found that surrogates with different densities behaved differently at lower velocities. A density more close to water, would mean that the models would likely act as 'tensile' plants even at lower speeds, thereby possibly making the drag coefficient development quite different, when considering how differently the Vogel exponent where in the 'bending' and 'tensile' regions.

PVC also has a much higher bending modulus. This difference in bending modulus was tried mitigated by reducing the thickness of the sheets, thereby reducing the flexural rigidity. Even so, the flexural ridity of the models were 4.4 and 2.7 times higher for the small and large model respectively. Flexural rigidity is likely most important for a 'bending' plant, as the flexural rigidity will determine how easily the plant reconfigures to the flow. Even so, flexibility has been shown

to be important when it comes to fluttering of flags, and cause an increase in drag compared to a solid, non-flexible sheet. When looking at the estimated 'tensile'-plant Vogel exponent of the small and large model, it seems that the large undulate model has a larger reduction in drag force compared to the small undulate model for both patch and blade scale. From the video footage, it was observed that the large undulate blades seemed to collapse on themselves. The ability to self-shade in this manner, will depend on flexibility. This phenomenon was only observed for the large blade, with relative lower flexibility due to its thickness being smaller compared to the width. Thus, it might be that a model with a flexural rigidity similar to the kelp, would collapse on to itself at even lower velocities, thereby reducing drag. On the other hand, the most likely quicker onset of 'tensile' blade behavior and fluttering, by having a lower density and flexural rigidity, might cause higher drag force than what was recorded in this master thesis. In conclusion, it is difficult to say how a model with correct stiffness and density would behave compared to the models used in this master thesis.

When it comes to the morphology of the models, the undulate model blade is much closer to the kelp, due to it having its characteristic undulate sides. However, the undulate models lack the ridges observed in the middle of the kelp blade. These have been found to reduce drag (Tani, 1988), in contrast to the undulation. The models also have a uniform thickness throughout, with only the sides of the undulate blade being somewhat thinner due to the process of making the undulation. This means that the real plant will have a higher flexural rigidity in the middle, while being much more flexible towards its ends and sides compared to the models. The higher flexural rigidity of the middle and ridges might make the real kelp more stable in the flow (Rominger and Nepf, 2014; Fryer et al., 2015).

The largest deviation from the real kelp for the models are the stipes, which have a width close to the radius of the real stipes, but a thickness of only 0.4 [mm], the same as the blade. The model stipes therefore have a much lower flexural and torsional rigidity, as was seen in Table 3.1. Some of the behaviors seen for the blades, might not have been possible if the stipes had had the correct rigidity. One example of such a behavior, is the observed pendulum motion for the flat blades.

4.7 Possible Error Sources

In accordance to what was discussed in Section 2.5.1, geometrical similarity also entails similarity in the flow field and environment. However, the depth of the tank was much smaller than the depth of the water where the seaweed farm will be, and the models much closer to the surface. In the laboratory, the distances between the water surface and the models, were approximately 236 [mm] and 250 [mm] for the simple and cylinder setup respectively. For comparison, the depths in which kelp are grown, could be between 2 and 8 [m]. However, the blades being dragged through the water did not seem to cause disturbance of the surface and no wave generation due to the presence of the models were observed. Similarly, it seems unlikely that there would be large interaction between the bottom of the tank and the models.

The grid on the other hand, did interfere with the surface and caused visible wave generation, especially at higher speeds. The same can be said for the profiled rod of the setup itself. Due to the grid, it became evident that the water height in the laboratory changes during the time the experiments were conducted. The force measured was filtered due to noise and vibrations. This is not likely to have influences the mean drag, as the lower frequencies were kept, but could have removed important physical phenomenons that occurred during the runs. Another observation, was that the models went from being transparent to somewhat white when exposed to water over time. This could have influenced their mechanical properties. When removed from water, the models eventually became transparent again.

In the previous sections it has been assumed that no force was lost through deformation of the profiled rod. However, as was seen from the very small drag forces measured for the cylinder setup, this might not be the case. Even so, the profiled rod is much shorter than the arms of the cylinder setup, and there is a possibility of friction in the hinge between the arms causing loss of force. The assumption of no force being used for deformation might therefore still be valid for the simple setup.

Chapter 5

Research Outcomes

5.1 Conclusions

There is large, visible difference between the undulate and flat blade model behaviors. This is the case on both blade and patch scale. The differences can be seen from the drag developments, with the drag force of the undulate model blade and undulate cluster being much larger than that of the flat blade and cluster. This was also evident from the drag coefficients, with the drag coefficient of the undulate model cluster being 3-4 times larger than that of the flat model cluster at higher velocities. However, it should be noted that this difference is likely somewhat overestimated, due to the underestimation of the wetted surface area of the undulate blades. The absolute value of the Vogel exponent was smaller for the undulate model in all instances, with the exception of large model cluster at higher velocities. This could mean that the undulate model reconfigures less to the flow than the flat model, and has less self-shading on both blade and patch scale.

From the video footage it was evident that the two models behaved differently when dragged trough the water, with the flat blade showing a pendulum motion, as well as being much less stable in general. The models also interact differently on patch scale. The flat models had a tendency of clumping together to form one thicker blade with only a few blades at each end of the cluster sometimes moving away from the rest. This behavior does not seem to fit real life kelp, as it would reduce the plants possibility for oxygen and nutrient uptake over its surface. The extensive self-shading of the patch would also likely hinder photosynthesis by, to some extent,

blocking sun light, thereby hindering the growth opportunities of the blades within the patch.

From the previously mentioned results from this study, it is seems that flat and undulate blade models cannot be used interchangeably and still be expecting the same results. Considering that the behavior shown by the flat blades does not seem like a satisfactory representation of the real kelp and its behavior, and that the undulate model had a shape closer to the real morphology of the kelp, it seems reasonable to assume that the undulate model behaves more closely to the real kelp.

Mechanical properties of models used in this master thesis differs from the biomechanical properties of the real kelp. Material density and flexural rigidity are likely to be the two very important difference. While the material density of the real kelp is close to that of water, the PVC used for the models have a density that is higher than water. This leads to the models acting more like 'bending' plants than as 'tensile' plants. The models first became aligned with the fluid flow at higher velocities. If the models have had a density closer to water and also correct flexural rigidity, it is expected that they would align with the flow at a lower velocity, and might also have experienced fluttering at a lower velocity. This might cause higher drag force, when considering studies on flags, than what was recorded for the models used in this master thesis. Meaning that, the use of these models might lead to underestimation of the drag force on a seaweed farm if used. It therefore seems important to compare the results from this master thesis with experiments conducted with similar models, but with correct material density and flexural rigidity before any definite statements of their behavior compared to the real kelp can be made.

Another major morphological and mechanical difference is with the stipe of the models. Their flexural and torsional rigidity are approximately 1/1000 and 1/10000 of the stipe of the real kelp. They therefore give almost no resistance to the movement of the models, compared to what the stipe of the kelp does. The model blades might have behaved differently, if their movements had been constricted by their stipes. Even so, the comparison of the flat blade model to the undulate blade model, should still be valid.

5.2 Recommendations for Future Work

The behavior of the models have not been directly compared to a real kelp. As the flat model does not seem to be a good surrogate, it is likely most beneficial to focus on the undulate model, and compare its behavior to the real kelp, and see if there is any significant differences. For these tests, using models with correct flexural rigidity and material density is recommended. This is because it will reduce the number of parameters that differ, thereby make comparison of the model and kelp easier. If it is not possible to get correct material density, then comparing the models with correct flexural rigidity to a real kelp might give information about how important having the correct density will be for replicating the behavior of the real kelp. It has been found that buoyancy, and therefore material density, is an important factor at low velocities (Paul and Henry, 2014). However, this might not be the case for higher velocities, which will be most important when considering the maximum drag force experienced by the seaweed farm. Therefore, it is of interest to find out if density also is important for higher velocities. Looking at the results, at the higher velocities the model is parallel with the flow, and therefore differences in densities between the model and kelp might not cause that big differences in drag force, and therefore should be investigated. After a good surrogate has been found on blade scale, its hydrodynamic properties on patch scale should be investigated and compared with a patch of real kelp.

Other parameters that should be investigated separately are; The effect the stipe has on the behavior of the blade, ridges in the middle of the blade and how blades of uniform thickness behaves compared to blades with changing thickness. Additionally, measurements of the flow velocity before and after the setup, as well as using dye or other methods for visualizing the flow, will be good tools when comparing the different model behaviors and evaluating any differences.

The models originally intended to be used for this master thesis, were going to be made out of polyurethane, a material with similar material density as *L. saccharina*. Molds for making these models were unfortunately not ready for use when the laboratory was available, but are now ready and can be used in future experiments. More details on these molds can be found in Appendix C. The polyurethane allows for different stiffnesses to be attained while maintaining

similar material density. These molds can therefore be used to see how the bending properties affects the drag. For 'bending' plants the flexibility, and consequently its ability to reconfigure to reduce its area as seen by the flow, is very important for its total drag (Nikora, 2010). However, this might not be as important for the 'tensile' plant as the drag force is expected to mainly come from skin drag. Making models with different bending moduli and therefore flexural rigidity will allow for investigation of how important it is to reproduce the flexural ridigity for a plant that can be described as a 'tensile' plant.

The experiments in this master thesis focused on blades that were parallel to each other on patch scale. It is however, of interests to see if undulate models, when placed in tandem, will experience the same anomalous hydrodynamic drafting such as that seen for interacting flapping flags in tandem (Ristroph and Zhang, 2008). If they do, this could be of high relevance for seaweed farms, as certain distances between the parallel ropes of the farm could lead to overall reduction of the total drag.

Only unidirectional flow without waves action were considered during this master thesis. However, Gaylord et al. (2001) found that transient loads could possibly be enlarged for tensile organism. If this is the case, then it could lead to the maximum total drag force for a patch, and consequently for a seaweed farm, to be grossly underestimated if not considered. The author therefore recommends taking this into considerations when planning future studies.

This master thesis has looked at drag force and visual cues when comparing the models. However, for a seaweed farm, even though the drag force is likely to be an important parameter when considering design, the flow structures around the kelp might be even more important for optimization of biomass production. The flow structures due to the plant-fluid and plant-plant interactions will determined the flux of nutrient and therefore be important in terms of growth. As a consequence, the author recommends future studies to focus more on visualizing the fluid flow and flow measurements, to ensure that this aspect is not neglected and is reproduces by the surrogates.

References

Albayrak, I., Nikora, V., Miler, O., and O'Hare, M. (2012). Flow-plant interactions at a leaf scale: effects of leaf shape, serration, roughness and flexural rigidity. *Research Across Boundaries*, 74(2):267–286.

Alben, S. (2009). Wake-mediated synchronization and drafting in coupled flags. *J. Fluid Mech.*, 641:489–496.

Bouma, T. J., De Vries, M. B., Low, E., Peralta, G., Tánczos, I. C., van de Koppel, J., and Herman, P. M. J. (2005). Trade-offs related to ecosystem engineering: A case study on stiffness of emerging macrophytes. *Ecology*, 86(8):2187–2199.

Buck, B. H. and Buchholz, C. M. (2005). Response of offshore cultivated laminaria saccharina to hydrodynamic forcing in the north sea. *Aquaculture*, 250(3):674–691.

Buckingham, E. (1914). On physically similar systems; illustrations of the use of dimensional equations. *Physical Review*, 4(4):345–376.

Carruthers, A. and Filippone, A. (2005). Aerodynamic drag of streamers and flags. *Journal of Aircraft*, 42(2):976–982.

Chakrabarti, S. K. (1994). *Offshore structure modeling*, volume 9 of *Advanced series on ocean engineering*. World Scientific, Singapore.

Chan, C.-X., Ho, C.-L., and Phang, S.-M. (2006). Trends in seaweed research. *Trends in Plant Science*, 11(4):165–166.

de Langre, E. (2008). Effects of wind on plants. *Annual Review of Fluid Mechanics*, 40:141–168.

Djenidi, L., Anselmet, F., Liandrat, J., and Fulachier, L. (1994). Laminar boundary layer over riblets. *Physics of Fluids*, 6(9):2993–2999.

Dubi, A. (1995). *Damping of Water Waves by Submerged Vegetation: A Case Study on Laminaria Hyperborea*. Thesis, University of Trondheim.

FAO (2016). The state of world fisheries and aquaculture 2016. Rome.

Farnell, D. J. J., David, T., and Barton, D. C. (2004). Coupled states of flapping flags. *Journal of Fluids and Structures*, 19(1):29–36.

Fryer, M., Terwagne, D., Reis, P. M., and Nepf, H. (2015). Fabrication of flexible blade models from a silicone-based polymer to test the effect of surface corrugations on drag and blade motion. *Limnology and Oceanography: Methods*, 13(11):630–639.

Gaylord, B. (2000). Biological implications of surf-zone flow complexity. *Limnology and Oceanography*, 45(1):174–188.

Gaylord, B., Hale, B. B., and Denny, M. W. (2001). Consequences of transient fluid forces for compliant benthic organisms. *Journal of Experimental Biology*, 204(7):1347–1360.

Gerard, V. A. (1987). Hydrodynamic streamlining of laminaria saccharina lamour. in response to mechanical stress. *Journal of Experimental Marine Biology and Ecology*, 107(3):237–244.

Ghisalberti, M. and Nepf, H. M. (2002). Mixing layers and coherent structures in vegetated aquatic flows. *Journal of Geophysical Research: Oceans*, 107(C2):3–1–3–11.

Harder, D., Speck, O., Hurd, C., and Speck, T. (2004). Reconfiguration as a prerequisite for survival in highly unstable flow-dominated habitats. *Published in cooperation with the Plant Growth Regulator Society of America and the International Plant Growth Substances Society*, 23(2):98–107.

Henry, P. Y. (2016). *Parametrisation of Aquatic Vegetation in Hydraulic and Coastal Research: The Importance of Plant Biomechanics in the Hydrodynamics of Vegetated Flows*. Thesis, NTNU Department of Marine Technology.

Henry, P.-Y. T. (2014). Bending properties of a macroalga: adaptation of peirce's cantilever test for in situ measurements of laminaria digitata (laminariaceae). *The American Journal of Botany*, 101(6):1050–1055.

Hoerner, S. F. (1965). *Fluid-dynamic drag : practical information on aerodynamic drag and hydrodynamic resistance*. S.F. Hoerner, Midland Park, N.J, 3rd edition.

Huang, I., Rominger, J., and Nepf, H. (2011). The motion of kelp blades and the surface renewal model. *Limnology and Oceanography*, 56(4):1453–1462.

Hurd, C. L., Stevens, C. L., Lava, B. E., Lawrence, G. A., and Harrison, P. J. (1997). Visualization of seawater flow around morphologically distinct forms of the giant kelp macrocystis integrifolia from wave-sheltered and exposed sites. *Limnology and Oceanography*, 42(1):156–163.

Johnson, A. S. and Koehl, M. A. R. (1994). Maintenance of dynamic strain similarity and environmental stress factor in different flow habitats: thallus allometry and material properties of a giant kelp. *Journal of Experimental Biology*, 195:381–410.

Johnson, M. F., Thomas, R. E., Dijkstra, J. T., Paul, M., Penning, W. E., and Rice, S. P. (2014). *Using surrogates, including scaling issues, in laboratory flumes and basins*, pages 23–41. IAHR Design Manual. CRC Press.

Koehl, M. and Alberte, R. (1988). Flow, flapping, and photosynthesis of Nereocystis leutkeana: a functional comparison of undulate and flat blade morphologies. *International Journal on Life in Oceans and Coastal Waters*, 99(3):435–444.

Koehl, M. A. (1999). Ecological biomechanics of benthic organisms: life history, mechanical design and temporal patterns of mechanical stress. *The Journal of experimental biology*, 202:3469–3476.

Krumhansl, K. A., Demes, K. W., Carrington, E., and Harley, C. D. G. (2015). Divergent growth strategies between red algae and kelps influence biomechanical properties. *American journal of botany*, 102(11):1938–1944.

Luhar, M. and Nepf, H. M. (2011). Flow-induced reconfiguration of buoyant and flexible aquatic vegetation. *Limnology and Oceanography*, 56(6):2003–2017.

Løvås, S. M. and Tørum, A. (2001). Effect of the kelp laminaria hyperborea upon sand dune erosion and water particle velocities. *Coastal Engineering*, 44(1):37–63.

Morris-Thomas, M. T. and Steen, S. (2009). Experiments on the stability and drag of a flexible sheet under in-plane tension in uniform flow. *Journal of Fluids and Structures*, 25(5):815–830.

Nikora, V. (2010). Hydrodynamics of aquatic ecosystems: An interface between ecology, biomechanics and environmental fluid mechanics. *River Research and Applications*, 26(4):367–384.

Parke, M. (1948). Studies on British Laminariaceae. I. Growth in Laminaria Saccharina Lamour. *J. Mar. Biol. Ass.*, 27(3):651–709.

Paul, M., Bouma, T., and Amos, C. (2011). Wave attenuation by submerged vegetation: combining the effect of organism traits and tidal current. *Marine Ecology Progress Series*, 444:31–41.

Paul, M. and Henry, P.-Y. T. (2014). Evaluation of the use of surrogate laminaria digitata in eco-hydraulic laboratory experiments. *Journal of Hydrodynamics, Ser.B*, 26(3):374–383.

Pierce, F. (1930). The "handle" of cloth as a masureable quantity. *Journal of the Textile Institute Transactions*, 21.

Ristroph, L. and Zhang, J. (2008). Anomalous Hydrodynamic Drafting of Interacting Flapping Flags. *Physical Review Letters*, 101(19):194502.

Rominger, J. T. and Nepf, H. M. (2014). Effects of blade flexural rigidity on drag force and mass transfer rates in model blades. *Limnology and Oceanography*, 59(6):2028–2041.

Rosman, J. H., Koseff, J. R., Monismith, S. G., and Grover, J. (2007). A field investigation into the effects of a kelp forest (Macrocystis pyrifera) on coastal hydrodynamics and transport. *Journal of Geophysical Research: Oceans*, 112(C2):C02016.

Rosman, J. H., Monismith, S. G., Denny, M. W., and Koseff, J. R. (2010). Currents and turbulence within a kelp forest (Macrocystis pyrifera): Insights from a dynamically scaled laboratory model. *Limnology and Oceanography*, 55(3):1145–1158.

Siniscalchi, F. (2012). *Hydrodynamics of flow-vegetation interactions at the scales of individual plant and plant patch*. Thesis, University of Aberdeen.

Skjermo, J., Forbord, S., Solbakken, R., Steinhoved, K., Handå, A., Arff, J., Broch, O., Reitan, K., Carvajal, A., Wolff, R., Aasen, I., Sandquist, J., Wittgens, B., Olsen, Y., Hartvig, C., and Rustad, T. (2014). A new Norwegian bioeconomy based on cultivation and processing of seaweeds: Opportunities and R&D.

Spurkland, T. and Iken, K. (2012). Seasonal growth patterns of Saccharina latissima (Phaeophyceae, Ochropytha) in glacially influenced subarctic estuary. *Phycological Research*, 60(4):261–275.

Statzner, B., Lamouroux, N., Nikora, V., and Sagnes, P. (2006). The debate about drag and reconfiguration of freshwater macrophytes: comparing results obtained by three recently discussed approaches. *Freshwater Biology*, 51(11):2173–2183.

Steen, S. (2014). *Lecture notes TMR7 Experimental methods in marine hydrodynamics*. Marine Technology Center, NTNU, Department of Marine Technology.

Stratigaki, V., Manca, E., Prinos, P., Losada, I., Lara, J., Sclavo, M., Amos, C., Caceres, I., Sanchez-Arcilla, A., and Stratigaki, V. (2011). Large-scale experiments on wave propagation over posidonia oceanica. *Journal of Hydraulic Research/Journal de Recherches Hydraulique*, 49:31–43.

Tani, I. (1988). Drag reduction by riblet viewed as roughness problem. *Proceedings of the Japan Academy, Series B*, 64(2):21–24.

Taylor, E. (1974). *Dimensional analysis for engineers*. Clarendon Press, Oxford.

Ugural, A. C. and Fenster, S. K. (2011). *Advanced mechanics of materials and applied elasticity*. Prentice Hall, Upper Saddle River, N.J, 5th edition.

United Nation, Department of Economic and Social Affairs, Population Division (2015). World Population Prospects: The 2015 Revision, Key Findings and Advance Tables.

Vettori, D. (2016). *Hydrodynamic Performance of Seaweed Farms: an Experimental Study at Seaweed Blade Scale*. Thesis, University of Aberdeen.

Vogel, S. (1983). *Life in moving fluids : the physical biology of flow*. Princeton paperbacks. Princeton University Press, Princeton, N.J.

Vogel, S. (1984). Drag and flexibility in sessile organisms. *American Zoologist*, 24(1):37–44.

Vogel, S. (1989). Drag and reconfiguration of broad leaves in high winds. *Journal of Experimental Botany*, 40(8):941–948.

Wainwright, S. A. (1976). *Mechanical design in organisms*. Edward Arnold, London.

Wang, X., Olsen, L. M., Reitan, K. I., and Olsen, Y. (2012). Discharge of nutrient wastes from salmon farms: environmental effects, and potential for integrated multi-trophic aquaculture. *Aquaculture Environment Interactions*, 2(3):267–283.

White, F. (2011). *Fluid Mechanics*. McGraw-Hill.

Zhang, J., Stephen, C., Albert, L., and Michael, S. (2000). Flexible filaments in a flowing soap film as a model for one-dimensional flags in a two-dimensional wind. *Nature*, 408(6814):835–839.

Zhu, L. and Peskin, C. S. (2003). Interaction of two flapping filaments in a flowing soap film. *Physics of Fluids*, 15(7):1954–1960.

Appendix A

Reynold Similitude

Scaling factor:

$$\lambda = \frac{L_F}{L_M} \tag{A.1}$$

Velocity:

$$Re = \frac{UL}{\upsilon} \tag{A.2}$$

$$U_F = \frac{\upsilon_F}{\upsilon_M}\frac{L_M}{L_F}U_M \tag{A.3}$$

$$U_F = \delta_\upsilon \lambda^{-1} U_M \tag{A.4}$$

Mass:

$$M = \rho_p V \tag{A.5}$$

$$M_F = \frac{\rho_{pF}}{\rho_{pM}}\left(\frac{L_F}{L_M}\right)^3 M_M \tag{A.6}$$

$$M_F = \frac{\rho_{pF}}{\rho_{pM}}\lambda^3 M_M \tag{A.7}$$

$$M_F = \delta_\rho \lambda^3 M_M \tag{A.8}$$

Time:

$$T = \frac{L}{U} \tag{A.9}$$

$$T_F = \frac{L_F}{L_M}\frac{U_M}{U_F}T_M \tag{A.10}$$

$$T_F = \delta_v^{-1}\lambda^2 T_M \tag{A.11}$$

Force:

$$[F] = MLT^{-2} \tag{A.12}$$

$$F_F = M_F L_F T_F^{-2} \tag{A.13}$$

$$F_F = (\delta_\rho \lambda^3 M_M)(\lambda L_M)(\delta_v^{-1}\lambda^2 T_M)^{-2} \tag{A.14}$$

$$F_F = \delta_\rho \delta_v^2 M_M L_M T_M^{-2} \tag{A.15}$$

$$F_F = \delta_\rho \delta_v^2 F_M \tag{A.16}$$

Elastic and bending modulus:

$$[E] = [E_b] = ML^{-1}T^{-2} \tag{A.17}$$

$$E_F = M_F L_F^{-1} T_F^{-2} \tag{A.18}$$

$$E_F = (\delta_\rho \lambda^3 M_M)(\lambda L_M)^{-1}(\delta_v^{-1}\lambda^2 T_M)^{-2} \tag{A.19}$$

$$E_F = \delta_\rho \delta_v^2 \lambda^{-2} M_M L_M^{-1} T_M^{-2} \tag{A.20}$$

$$E_F = \delta_\rho \delta_\upsilon^2 \lambda^{-2} E_M \tag{A.21}$$

Second moment of area:

$$[I] = L^4 \tag{A.22}$$

$$I_F = L_F^4 \tag{A.23}$$

$$I_F = (\lambda L_M)^4 \tag{A.24}$$

$$I_F = \lambda^4 L_M^4 \tag{A.25}$$

$$I_F = \lambda^4 I_M^4 \tag{A.26}$$

Flexural ridigity/hydroelasticity:

$$[J] = ML^3 T^{-2} \tag{A.27}$$

$$J_F = M_F L_F^3 T_F^{-2} \tag{A.28}$$

$$J_F = (\delta_\rho \lambda^3 M_M)(\lambda L_M)^3 (\delta_\upsilon^{-1} \lambda^2 T_M)^{-2} \tag{A.29}$$

$$J_F = \delta_\rho \delta_\upsilon^2 \lambda^2 M_M L_M^3 T_M^{-2} \tag{A.30}$$

$$J_F = \delta_\rho \delta_\upsilon^2 \lambda^2 J_M \tag{A.31}$$

Appendix B

Froude Similitude

Scaling factor:

$$\lambda = \frac{L_F}{L_M} \tag{B.1}$$

Velocity:

$$Fr = \frac{U}{\sqrt{gL}} \tag{B.2}$$

$$U_F = \sqrt{\frac{L_F}{L_M}} U_M \tag{B.3}$$

$$U_F = \lambda^{1/2} U_M \tag{B.4}$$

Mass:

$$M = \rho_p V \tag{B.5}$$

$$M_F = \frac{\rho_{pF}}{\rho_{pM}} \left(\frac{L_F}{L_M} \right)^3 M_M \tag{B.6}$$

$$M_F = \frac{\rho_{pF}}{\rho_{pM}} \lambda^3 M_M \tag{B.7}$$

$$M_F = \delta_\rho \lambda^3 M_M \tag{B.8}$$

Time:

$$T = \frac{L}{U} \tag{B.9}$$

$$T_F = \frac{L_F}{L_M}\frac{U_M}{U_F}T_M \tag{B.10}$$

$$T_F = \lambda^{1/2} T_M \tag{B.11}$$

Force:

$$[F] = MLT^{-2} \tag{B.12}$$

$$F_F = M_F L_F T_F^{-2} \tag{B.13}$$

$$F_F = (\delta_\rho \lambda^3 M_M)(\lambda L_M)(\lambda^{1/2} T_M)^{-2} \tag{B.14}$$

$$F_F = \delta_\rho \lambda^3 M_M L_M T_M \tag{B.15}$$

$$F_F = \delta_\rho \lambda^3 F_M \tag{B.16}$$

Elastic and bending modulus:

$$[E] = [E_b] = ML^{-1}T^{-2} \tag{B.17}$$

$$E_F = M_F L_F^{-1} T_F^{-2} \tag{B.18}$$

$$E_F = (\delta_\rho \lambda^3 M_M)(\lambda L_M)^{-1}(\lambda^{1/2} T_M)^{-2} \tag{B.19}$$

$$E_F = \delta_\rho \lambda M_M L_M^{-1} T_M^{-2} \tag{B.20}$$

$$E_F = \delta_\rho \lambda E_M \tag{B.21}$$

Moment of inertia:

$$[I] = L^4 \tag{B.22}$$

$$I_F = L_F^4 \tag{B.23}$$

$$I_F = (\lambda L_M)^4 \tag{B.24}$$

$$I_F = \lambda^4 L_M^4 \tag{B.25}$$

$$I_F = \lambda^4 I_M^4 \tag{B.26}$$

Flexural ridigity/hydroelasticity:

$$[J] = ML^3 T^{-2} \tag{B.27}$$

$$J_F = M_F L_F^3 T_F^{-2} \tag{B.28}$$

$$J_F = (\delta_\rho \lambda^3 M_M)(\lambda L_M)^3 (\lambda^{1/2} T_M)^{-2} \tag{B.29}$$

$$J_F = \delta_\rho \lambda^5 M_M L_M T_M \tag{B.30}$$

$$J_F = \delta_\rho \lambda^5 J_M \tag{B.31}$$

Appendix C

Surrogate Models Made with Molds

For this master thesis, two molds made out of aluminum were prepared. The models made from these molds can be seen in Figure C.1. Originally these were planned to be used to make polyurethane models and look at how they behaved when dragged through water, similarly to what was done with the PVC models.

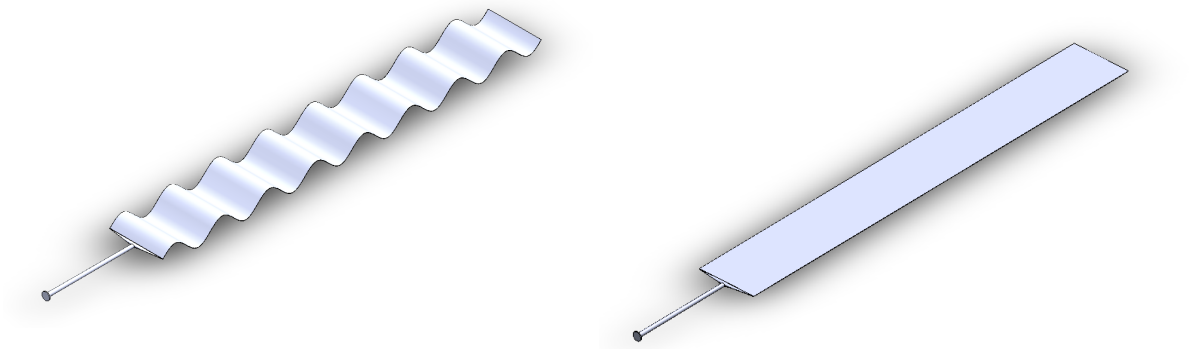

(a) Wave amplitude remains the same throughout the model

(b) Wave amplitude equal to zero - flat blade

Figure C.1: Models that can be made with available aluminum molds.

These models can be made by using a method similar to how supervisor Pierre-Yves Henry made his silicone models from a *Laminaria digitata* mold, see Figure C.2. The polyurethane components should be well mixed before inserting the mix into a vacuum chamber to expand the air bubbles within to reduce the amount of air in the final product. A motor can be used to remove the air from the chamber. Afterwards, the mix is removed from the vacuum chamber and the mold inserted with tubing from the bottom of the mold being connected to the bottom

of the vacuum chamber. This inlet has a tube connected to it, that can be inserted into the mix, placed outside of the vacuum chamber. The inlet connected to the mold should then subsequently be opened. The mix will then be sucked into the mold, due to the difference in pressure between the ambient environment and the vacuum chamber. After the mold has been filled, it should be put into ovens for curing of the polyurethane.

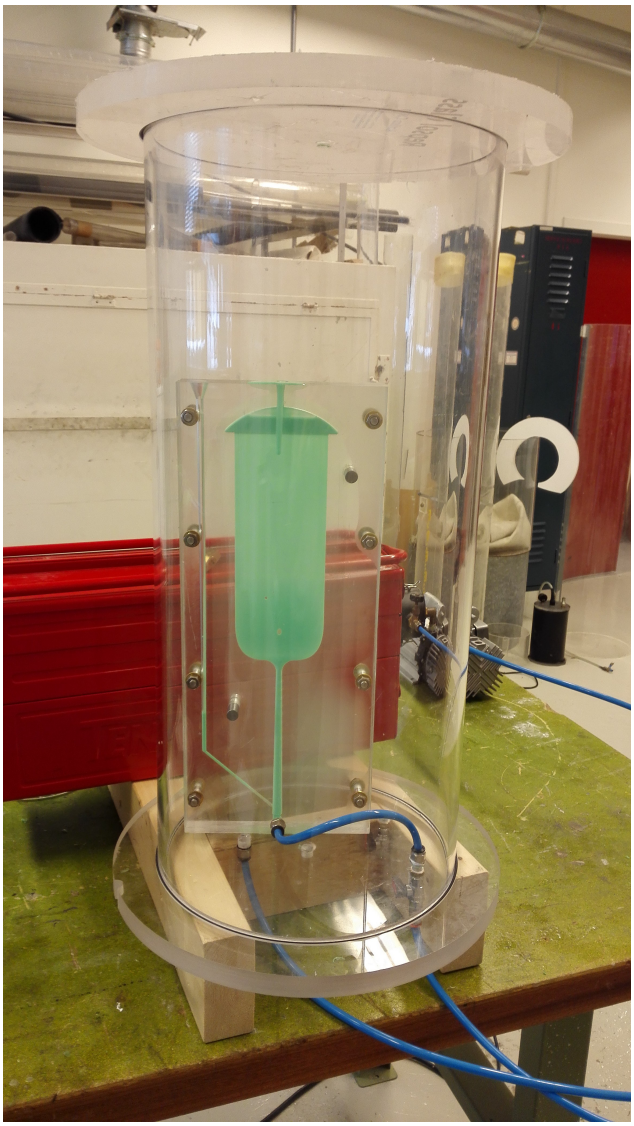

Figure C.2: Silicone-filled *L. digitata* mold in vacuum chamber.